Master's thesis

NTNU
Norwegian University of Science and Technology
Faculty of Natural Sciences
Department of Physics

Kristian Hjorth

Using Photon Entanglement as a Fundamental Resource in Experimental Physics

Master's thesis in Applied Physics and Mathematics
Supervisor: Bo-Sture Skagerstam
September 2019

NTNU
Norwegian University of
Science and Technology

Kristian Hjorth

Using Photon Entanglement as a Fundamental Resource in Experimental Physics

Master's thesis in Applied Physics and Mathematics
Supervisor: Bo-Sture Skagerstam
September 2019

Norwegian University of Science and Technology
Faculty of Natural Sciences
Department of Physics

NTNU
Norwegian University of
Science and Technology

Preface

This thesis is submitted for the degree of *Master of Science in Applied Physics and Mathematics* at the Norwegian University of Science and Technology (NTNU). It was written during the summer of 2019, and is the culmination of my work as a Master student at the group of Dr. Rupert Ursin within the Institute for Quantum Optics and Quantum Information (IQOQI) in Vienna.

The thesis work has been a deep dive into the field of quantum optics and photon entanglement. With this as a starting point, I present preliminary results from two experiments I have been so lucky as to contribute to, where photon entanglement has been explored as a source for metrology and for quantum key distribution. Sections 2.1.1, 2.2.1, 2.3, 3.1.1, 3.2, 3.4 and 3.4.1 are partly or entirely based on my project thesis: *"Theoretical background of a Bell inequality test for polarization and energy-time entangled photons"* [1], written during January 2019.

I would like to express my gratitude to a number of people for making this thesis possible:

- Dr. Rupert Ursin, for accepting me into his group and for supporting a fun and relaxed environment to do research.
- Lukas Bulla, for inviting me to join in on his experiments and trusting me not to mess up his PhD work.
- Prof. Bo-Sture Skagerstam, for spiking my interest within quantum optics and for making it possible to write this thesis abroad.
- Ulrich Galander, Domenico Ribezzo and Sebastian Neumann, for lending us the source and detector modules that were used in Chapter 4.
- Oskar Kohout and Robert Kindler, for their help and contributions to the free-space link I describe in Chapter 5.
- My family, for giving me the opportunity in life to pursue what I find most exciting. Thank you.

Kristian Hjorth
Vienna, Austria
September 2019

Abstract

In this thesis, I describe two experiments related to the use of entangled photon pairs within metrology and quantum key distribution (QKD). In relation to metrology, we investigate a clock synchronization scheme based on the coincidence detection of entangled photons. With the high pair rates of modern entangled photon sources, timing uncertainties due to jitter in the photon detectors and data acquisition system can be made almost arbitrarily small. We show that our setup is able to measure the time drift between remote clocks within $1\,\mathrm{ps}$ over sampling times smaller than $1\,\mathrm{s}$, essentially being limited by the $1\,\mathrm{ps}$ counting resolution of our time tagger units. Within the laboratory frame, we perform a proof-of-principle test, intended to explore the synchronization scheme as a tool for measuring gravitational time dilation. This inevitably failed due to the required stability of our rubidium standard atomic clocks. Nevertheless, the synchronization scheme is shown to accurately measure the frequency instability of our timing standards, demonstrating that the scheme is feasible to work over larger height differences or with more stable clocks. Additionally, as a sanity check of the photon source, the presence of polarization entanglement was verified with a Bell inequality test showing a maximal violation of $S = 2.81 \pm 0.01$.

The second experiment I describe is dedicated to the implementation of a free-space QKD link, stretching $10.2\,\mathrm{km}$ across the skyline of Vienna. We investigate here a noise robust QKD protocol, based on hyperentangled photon states analyzed with a post-selection free Franson interferometer. With proof-of-principle measurements from the lab, Franson interference is demonstrated with a visibility of 92%. I further discuss the design choices that were made in order to prepare the receiver module for a free-space link. In terms of this, ensuring the transmission stability of the link despite the effects of atmospheric turbulence is a prominent engineering challenge. The magnitude of turbulence across our link is assessed with a differential image motion monitor (DIMM) integrated in the receiver module. For the long-term stability of the link, I present a bidirectional tracking scheme, correcting the angle of our transmitter module and receiver module in a closed feed-back loop to ensure optimal transmission stability.

Sammendrag

I denne masteroppgaven beskriver jeg to ulike eksperimenter relatert til bruken av sammenfiltrede fotonpar for metrologi og kvantenøkkeldistribusjon. Innenfor metrologi undersøkes et oppsett for å synkronisere klokker basert på koinsidensmålingen av sammenfiltrede fotoner. Med dagens lyssterke kilder av sammenfiltrede fotoner kan usikkerheten i deteksjonstid fra støy i fotondetektoren og signalbehandlingselektronikken gjøres nærmest vilkårlig lav. Vi viser at oppsettet vårt er i stand til å måle avviket mellom to uavhengige klokker med en presisjon innenfor $1\,\mathrm{ps}$ over måleperioder mindre enn $1\,\mathrm{s}$, hvor tidsoppløsningen til den elektroniske tidtakeren på $1\,\mathrm{ps}$ er den fundamentale flaskehalsen. I et konseptbevis tester vi dette prinsippet i laboratoriet, med en intensjon om å måle tidsdilatasjonen fra gravitasjonsfeltet til jorden. Dette feilet på grunn av stabiliteten som krevdes av de rubidium-baserte atomklokkene. Likevel viser eksperimentet at vi nøyaktig kan måle frekvensavviket til de to klokkene, noe som demonstrerer at forsøket kan fungere over større høydeforskjeller eller med mer stabile klokker. For å verifisere at kilden vår produserer sammenfiltrede fotoner viser vi i tillegg et maksimalt brudd med Bells ulikhet på $S = 2.81 \pm 0.01$.

Det andre eksperimentet jeg beskriver er dedikert til oppsettet av en protokoll for kvantenøkkeldistribusjon over en atmosfærisk forbindelse, som strekker seg $10.2\,\mathrm{km}$ langs himmelen over Wien. Her undersøker vi en støy-robust protokoll, basert på sammenfiltrede fotonpar i flere frihetsgrader, som vi analyserer med et modifisert Franson interferometer. Oppsettet ble først implementert i laboratoriet, hvor vi kunne påvise interferenskontrast på 92%. Videre diskuterer jeg designvalgene som har blitt gjort for å forberede oppsettet for bruk i en atmosfærisk forbindelse. En fremtredende ingeniørutfordring i forbindelse med dette er å sørge for stabil signaloverføring tross påvirkningen fra en turbulent atmosfære. Omfanget av den atmosfæriske påvirkningen på signalet kvantifiseres ved hjelp av en «differential image motion monitor» (DIMM), som er bygd inn i oppsettet til mottakermodulen. For stabiliteten til signaloverføringen over lengre tidsperioder ble et to-veis «tracking»-system utviklet, som kontinuerlig korrigerer vinkelen til sender- og mottakermodulen for å optimere signalstyrken.

Contents

Preface **2**

Abstract **3**

Sammendrag **5**

Table of Contents **9**

List of Abbreviations **10**

1 Introduction **11**

2 Theoretical Framework **13**

2.1 The Quantum Nature of Light 13

2.1.1 States in Hilbert Space 14

2.2 The Photon as Information Carrier 16

2.2.1 Photon Polarization 16

2.2.2 Spectral and Temporal Modes 19

2.2.3 Spatial and Momentum Modes 20

2.3 Quantum Entanglement in Two-Photon Systems 20

3 Toolbox for Two-Photon Entanglement Experiments **25**

3.1 Producing Entangled Photon Pairs 25

3.1.1 Spontaneous Parametric Down-Conversion 25

3.1.2 Entanglement from SPDC 28

3.2 The Sagnac Source 29

3.3 Polarization Analyzing Module 30

3.4 The Franson Interferometer 32

3.4.1 The Post-Selection Free Franson Interferometer 34

4 Feasibility of Measuring Time Dilation with the Two-Photon Coincidence Peak 37

4.1 Background: Time Dilation and Timing Standards 38

4.2 Assessing Clock Stability 39

4.3 Synchronizing Clocks with Entangled Photons 40

4.3.1 Temporal Correlations in SPDC Pairs 40

4.3.2 Timing Resolution of Photon Detection 41

4.3.3 Identifying the Timing Offset 42

4.4 Setup and Components 43

4.5 Performance Test of the Source and Data Acquisition System 45

4.5.1 Measuring the Timing Jitter 45

4.5.2 Test of Polarization Entanglement 46

4.6 Test of Clock Synchronization with SPDC 49

4.7 Discussion 53

5 Establishing a High-Dimensional Free-Space QKD Link **55**

5.1 Improved Noise Resilience from a Higher-Dimensional State Space . . . 56

5.2 Proof-of-Principle: Franson Interference in the Lab 57

5.2.1 A Type-2 Sagnac Source 57
5.2.2 Implementation of a Post-Selection Free Franson Interferometer . 58
5.2.3 Stabilizing the Interferometer Path Length 58
5.2.4 Data Acquisition 60
5.2.5 Experimental Routines 60
5.2.6 Demonstration of Franson Interference 62
5.3 Free-Space Considerations 62
5.3.1 Transmission of Light in Atmospheric Conditions 63
5.3.2 Differential Image Motion Monitoring (DIMM) 64
5.4 Setup and Design Choices 65
5.4.1 The Free-Space Link 65
5.4.2 Transmitter Optics 65
5.4.3 Receiver Optics 66
5.4.4 Bidirectional Tracking 68
5.4.5 The DIMM Setup 69
5.4.6 Test of the Tracking and DIMM Setup 70

6 Summary and Outlook **73**

Bibliography **79**

A Some Classical Optics **81**

B Tracking Software **83**

List of Abbreviations

AoA — angle of arrival

BS — beam splitter

CCD — charge-coupled device

CMOS — complementary metal-oxide semiconductor

cps — counts per second

cw — continuous-wave

DIMM — differential image motion monitor

DOF — degree(s) of freedom

EPS — entangled photon source

FC — fiber coupler

FoV — field of view

FWHM — full-width half-maximum

GPS — global positioning system

HWP — half-wave plate

LED — light-emitting diode

LEO — low earth orbit

MUB — mutually unbiased bases

PBS — polarizing beam splitter

PC — polarization controllers

QIS — quantum information science

QKD — quantum key distribution

QWP — quarter-wave plate

rms — root mean square

SM — single-mode

SNSPD — silicon nanowire single photon detector

SPCM — single-photon counting module

SPDC — spontaneous parametric down-conversion

TM — temporal mode

Chapter 1

Introduction

Characterized by its many counterintuitive phenomena, quantum mechanics opens up a strange world in which particles act as waves, where its attributes such as position, momentum and energy must be described by superpositions over all possible states, and where probabilities govern the outcome of measurements. Nevertheless, its predictions led to the development of breakthrough technologies such as the laser, transistor and atomic clock, without which fibre-optic networks, modern computers and precise GPS navigation tools would not have existed. To date, our continued improvement in the engineering of quantum states on the single particle level promise a new wave of applications finding its way into mature technology.

A concept that will be central in the next generation of quantum technologies is a phenomena known as quantum entanglement. Quantum entangled states are systems of two or more particles, where the properties of the particles are completely unknown until a measurement of either particle determines the state of both. As the phenomena persists regardless of their physical separation, this leads to surprising and controversial conclusions such as the apparent non-local (faster-than-light) interaction between the two particles, which is why the phenomena historically has played a central role in the interpretation of quantum mechanics. Today, entanglement is more precisely considered in terms of non-classical correlations — i.e. correlations that can't be explained without quantum mechanics — and can be experimentally verified by violating so-called *Bell inequalities*, devised by John S. Bell in 1964 [2]. Since then, numerous experiments have verified the existence of quantum entanglement in a wide range of systems, including photons [3–12], cold atoms [13, 14] and superconducting circuits [15, 16]. Although no superluminal interaction is needed to explain these experiments, the alternative interpretation states that the common sense notion of *realism* — that a physical system holds definite properties independent of our observation — must break down. Whichever it is, quantum entangle-

ment certainly places high on the hierarchy of exotic quantum phenomenons. Despite this, it is a cornerstone in promising technologies such as quantum computing and quantum key distribution (QKD).

Early stage quantum phenomena tests has predominantly been carried out on photon states. This can in part be traced to their ease of production, but maybe more importantly to their weak interactions with surrounding environment, making it far easier to manipulate and conserve photonic quantum states than with alternative systems. Consequently, the first wave of new generation quantum technologies is likely to be based on quantum optics, as the barrier between the shielded environment of the laboratory and the real world is far smaller. Perhaps the most prominent of these technologies is quantum key distribution, where the quantum mechanics of photon states are utilized to establish the distribution of unconditionally secure encryption keys between two parties.

Within this thesis, I've explored experimental methods to produce, manipulate and measure entangled two-photon states in multiple degrees of freedom. With this as a basis, I give insight into two experiments I've contributed to at the Institute for Quantum Optics and Quantum Information (IQOQI) in Vienna over the last year, one of which is related to entanglement within metrology, the other to QKD.

The thesis will be structured accordingly: First, I present a general introduction to the theory of quantum mechanics, focusing on the photon, its degrees of freedom and the concept of entanglement in photon pairs. Chapter 3 will be dedicated to experimental procedures for producing and verifying two-photon entanglement, including the theoretical framework of spontaneous parametric down-conversion (SPDC), the Sagnac source, polarization analyzing modules and the Franson interferometer. In Chapter 4, I present the first of two experiments, where I explore the intrinsic time correlations of entangled photon pairs and the feasibility of using it as a tool for measuring gravitational time dilation. Finally, in Chapter 5 I describe preliminary results in the attempt to establish a $10.2\,\mathrm{km}$ long free-space link across the skyline of Vienna, in which photons entangled in both the polarization and temporal degree of freedom are envisioned as information carriers in a QKD protocol.

Chapter 2

Theoretical Framework

In this thesis, the concept of quantum entanglement in two-photon systems plays a fundamental role. An understanding of this phenomena requires a brief introduction into the mathematical framework of quantum mechanics. I therefore use this chapter to present the most important building blocks to the concepts we will use to describe quantum optics experiments, focusing on the photon and its potential in the point of view of quantum information science (QIS). The contents of this chapter are firmly rooted in a multitude of standard quantum optics textbooks [e.g. 17–21].

2.1 The Quantum Nature of Light

The physical theory of light has seen drastic paradigm shifts throughout history. In the classical theory of electromagnetism, light takes the shape of waves, propagating through space according to Maxwell's set of equations [22]. With Einsteins bold interpretation of the photoelectric effect in one of his 1905 *Annus Mirabilis*-papers however [23], a new picture of light emerged, now consisting of discrete quantas of particles called photons. This new picture marked the advent of quantum mechanics, and with it a quite confusing view of light, exhibiting something of both a wave-like and particle-like nature. This *wave-particle dualism* becomes evident in the standard *quantization* procedure of the electromagnetic field, where the classical fields of Maxwell's equations are quantized into quantum mechanical field operators. The essence of this procedure is to expand the electromagnetic field into a set of orthonormal field modes that are solutions to the Maxwell equations. For a freely propagating electric field in space-time, denoted by position and time coordinates $(\mathbf{r}, t)$, these modes are plane waves with different momenta $\mathbf{k}$, frequency ω and polarization λ, and the electric field operator $\hat{\mathbf{E}}(\mathbf{r}, t)$ takes the form (see

e.g. [17, 24])

$$\begin{aligned}\hat{\mathbf{E}}(\mathbf{r},t) &= \hat{\mathbf{E}}^{+}(\mathbf{r},t) + \hat{\mathbf{E}}^{-}(\mathbf{r},t) \\ &= i\frac{1}{(2\pi)^3}\int d^3\mathbf{k}\sum_{\lambda}\sqrt{\frac{1}{2}\hbar\omega_k}(\epsilon_{\mathbf{k}\lambda}\hat{a}_{\mathbf{k}\lambda}e^{i(\mathbf{kr}-\omega_k t)} - \hat{a}^{\dagger}_{\mathbf{k}\lambda}\epsilon^{*}_{\mathbf{k}\lambda}e^{-i(\mathbf{kr}-\omega_k t)}),\end{aligned} \tag{2.1}$$

where $\hat{\mathbf{E}}^{+}(\mathbf{r},t)$ and $\hat{\mathbf{E}}^{-}(\mathbf{r},t)$ denotes the field spectra with positive and negative frequency modes. With this equation, some important properties of photons can be deduced. First of all, the photon as a concept arise from the association of the field mode amplitudes $\hat{a}_{\mathbf{k}\lambda}$ and $\hat{a}^{\dagger}_{\mathbf{k}\lambda}$ with the respective creation and annihilation of photon states with momenta $\mathbf{k}$ and polarization λ. This motivation comes from the expression for the Hamiltonian energy, which with the current form of the electric field takes the form [21]

$$\hat{\mathbf{H}} = \int d^3\mathbf{k}\sum_{\lambda}\hbar\omega_k\hat{a}^{\dagger}_{\mathbf{k}\lambda}\hat{a}_{\mathbf{k}\lambda}. \tag{2.2}$$

The energy increases with discrete increments of $\hbar\omega_k$ — the energy of one photon — times the operator combination $\hat{a}^{\dagger}_{\mathbf{k}\lambda}\hat{a}_{\mathbf{k}\lambda}$, which effectively counts the number of photons in the $(\mathbf{k},\lambda)$ mode. The wave-particle dualism is then beautifully described within Eq. (2.1). The wave-like properties are encoded in the field modes, while the particle-like nature is encoded in the creation and annihilation operators.

Secondly, from Eq. (2.1) we can read of the four independent degrees of freedom of the photon, namely the polarization λ — arising from the independent directions of oscillation encoded in $\epsilon_{\mathbf{k}\lambda}$ — and the three components of the momentum vector $\mathbf{k}$, which we due to the relation $\omega = c|\mathbf{k}|$ can divide into its transverse parts $\mathbf{k}^{\perp}$ and the frequency ω. These independent degrees of freedom are the choices we have to encode information in photons. How to produce, manipulate and measure these properties are therefore important research areas within quantum information science.

2.1.1 States in Hilbert Space

We refer to field modes with distinct polarization, frequency and momenta as photon states. As long as no interactions regarding photon creation and annihilation is involved, manipulation of photon states can be described within the framework of non-relativistic quantum mechanics. Formally, this mathematical formalism is that of vectors and vector operations in the linear unitary vector space called Hilbert space, $\mathcal{H}$. A single photon state is labeled by Dirac vectors $|\Psi\rangle = |\lambda,\omega,\mathbf{k}^{\perp}\rangle$, where we demand that the projection of $|\Psi\rangle$ onto its adjoint vector $\langle\Psi| = |\Psi\rangle^{*}$ yields 1, i.e. that the state is normalized. This requirement is

connected to an essential feature of quantum mechanics, namely its probabilistic nature. This is in turn reflected in Born's rule for quantum measurements, which states that the probability of a measurement of the initially prepared state $|\Psi\rangle$ to yield a different state $|\Phi\rangle$ is obtained by the square-modulo of the projection

$$P_{\Psi}(\Phi) = |\langle\Phi|\Psi\rangle|^2. \tag{2.3}$$

An essential feature of Dirac vectors is that they are basis-independent, and a state $|\Psi\rangle$ may therefore always be decomposed into a set of orthonormal basis vectors $\{|\psi_n\rangle\}$

$$|\Psi\rangle = \sum_n c_n |\psi_n\rangle, \tag{2.4}$$

where $c_n = \langle\psi_n|\Psi\rangle$ are complex probability amplitudes. The equivalence of different basis choices is a key concept in quantum mechanics, as will be evident throughout this chapter.

The Density Operator The formalism of Dirac vectors in Hilbert space is sufficient to describe quantum mechanics in terms of pure quantum states. An experimenter nevertheless has to deal with statistical uncertainties in how a state is prepared, and how it is altered throughout the experiment. Whenever the experimenter lacks complete knowledge on the system, it is better described as a statistical ensemble of pure quantum states, so-called *mixed states*. This prompts the use of the density operator

$$\hat{\rho} = \sum_n p_n |\psi_n\rangle\langle\psi_n|, \tag{2.5}$$

which describes a sum of pure quantum states $|\psi_n\rangle$, with corresponding weights p_n representing the statistical distribution of the ensemble. The projection operators $\hat{\mathcal{P}}_n = |\psi_n\rangle\langle\psi_n|$ can be identified as measurement operations on the prepared state, querying whether or not the state is in the basis state $|\psi_n\rangle$. The expectation value of such a measurement on the mixed state described by $\hat{\rho}$ is found by the tracing operation

$$\langle\hat{\mathcal{P}}_n\rangle = P_{\hat{\rho}}(\psi_n) = \mathrm{Tr}\{\hat{\rho}\hat{\mathcal{P}}_{\mathrm{n}}\}, \tag{2.6}$$

returning the weight p_n.

2.2 The Photon as Information Carrier

Photons are in many ways the ultimate information carrier of our world. For one part, it is hard to conceive a faster way of transferring information than by the speed of light. Adding to this, the four degrees of freedom (DOF) of the photon provide ample opportunities for information encoding, which due to their weak interactions with the environment make it possible to transmit states over long distances without the information encoded in them being destroyed along the way. Due to this, light is already extensively used as information carrier in modern telecommunication technologies, such as fiber-optic networks and Wi-Fi, connecting all laptops and smartphones to the internet. Although these devices rely on the principles of quantum mechanics to work, the information encoding itself uses purely classical properties of light. The potential of photons as information carriers goes much further than this however, and this is in large due to its quantum nature.

To see how the quantum nature of light can be exploited, we must understand the special characteristics of the independent DOF. Generally, the complete Hilbert space of the photon is the composite of the respective Hilbert spaces of each DOF

$$\mathcal{H} = \bigotimes_i \mathcal{H}_i = |\lambda\rangle \otimes |\omega\rangle \otimes |\mathbf{k}^{\perp}\rangle \,, \tag{2.7}$$

and we may therefore discuss photon states like $|\lambda\rangle$ on its own, implying that different polarization states are equal in all other regards.

2.2.1 Photon Polarization

The polarization of the photon arise from a freedom in the direction of oscillation of the electromagnetic field. This freedom makes up a two-dimensional state space, and can therefore always be represented as a *superposition* of two basis vectors. A common choice is the horizontal $|H\rangle$ and vertical $|V\rangle$ linear polarization states, which makes up what one may define as a *computational basis*. These two states are orthonormal, meaning that we can use Eq. (2.4) to form a completely general polarization state

$$|\Psi\rangle = c_0 \, |H\rangle + c_1 \, |V\rangle \,. \tag{2.8}$$

This type of two-level state holds a special place in quantum information science, as it represents a *qubit* — the quantum analog to a classical bit of information. This is easily seen by identifying the horizontal state with $|0\rangle$ and the vertical state with $|1\rangle$. The qubit state is however distinctly different from the classical bit, as it is able to represent both states simultaneously.

The space of basis choices for the two-level qubit state is elegantly visualized by the Bloch sphere, Fig. 2.1. The normalization of the complex coefficients $|c_0|^2 + |c_1|^2 = 1$ implies that the polarization states can be represented as points on the surface of a sphere, and can thus be parameterized by polar angles $(2\theta, \phi)$

$$|\Psi\rangle = \cos\theta\,|H\rangle + e^{i\phi}\sin\theta\,|V\rangle\,. \tag{2.9}$$

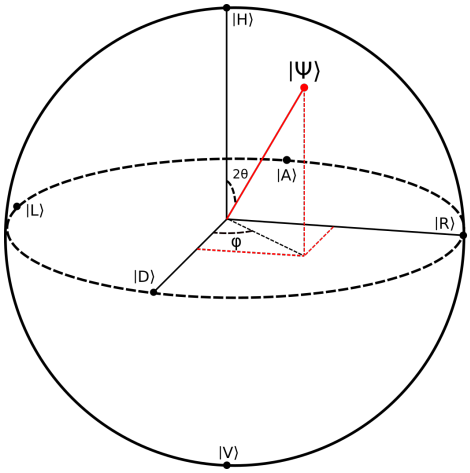

Figure 2.1: The Bloch sphere serves as a geometrical illustration of the space of pure polarization states.

Convention is to define the three axes of the Bloch sphere as the eigenvectors of the three Pauli matrices $\{\hat{\sigma}_1, \hat{\sigma}_2, \hat{\sigma}_3\}$. These three sets of eigenvectors make up three basis choices, known as the horizontal-vertical (H/V) and diagonal-antidiagonal (D/A) linear polarization bases and the left-right (L/R) circular polarization basis. The relation of the two new basis choices to the computational basis is

$$|D\rangle = \frac{1}{\sqrt{2}}(|H\rangle + |V\rangle) \qquad |A\rangle = \frac{1}{\sqrt{2}}(|H\rangle - |V\rangle) \tag{2.10}$$

$$|R\rangle = \frac{1}{\sqrt{2}}(|H\rangle + i\,|V\rangle) \qquad |L\rangle = \frac{1}{\sqrt{2}}(|H\rangle - i\,|V\rangle) \tag{2.11}$$

A central feature of the H/V, D/A and L/R states is that they form a set of *mutually unbiased bases* (MUBs). The outcome of a state measured in a MUB is completely random, hence destroying the information kept in the prior prepared state. This is quickly seen by doing a projective measurement of the state $|D\rangle$ onto the H/V basis, yielding

$$P_D(H) = |\langle D|H\rangle|^2 = \frac{1}{2}, \qquad P_D(V) = |\langle D|V\rangle|^2 = \frac{1}{2} \tag{2.12}$$

indicating that the outcome is completely random. More general polarization measurements can be described by the operator

$$\hat{\sigma}_n = |\mathbf{n}+\rangle\langle\mathbf{n}+| - |\mathbf{n}-\rangle\langle\mathbf{n}-|, \tag{2.13}$$

where $|\mathbf{n}+\rangle$ and $|\mathbf{n}-\rangle$ are the two possible eigenstates of a measurement along the direction $\mathbf{n} = (\sin\phi\sin 2\theta, \cos\phi\sin 2\theta, \cos 2\theta)$ on the Bloch sphere

$$|\mathbf{n}+\rangle = \begin{pmatrix} \cos\theta \\ \sin\theta e^{i\phi} \end{pmatrix}, \qquad |\mathbf{n}-\rangle = \begin{pmatrix} \sin\theta \\ -\cos\theta e^{i\phi} \end{pmatrix}. \tag{2.14}$$

The concept of MUBs is key to many QKD protocols, naming the standard BB84-protocol [25] as an example, where a random change in the preparation and measurement basis of the photon is used to place bounds on the information eavesdroppers can extract. Perhaps even more fascinating is the concept of *quantum erasure* of *which-path* information. Interference caused by multiple photon pathways, for example through a Young double-slit setup, can be erased by marking the separate paths by the photons polarization (see e.g. [26]). Removing the which-path information, e.g. by projecting the polarization onto a MUB, then restores the interference. This concept is applied in the post-selection free Franson interferometer, described in Section 3.4.1, which we in turn use in our experimental setup in Chapter 5.

Traditionally, quantum optics experiments have focused mainly on the polarization state-space of photons. Partly, this can be attached to the simplicity of the two-dimensional state-space, while mainly it has to do with the ease of which polarization states can be manipulated and measured. Any measurement basis may be realized by a combination of birefringent wave-plates and a polarizing beam splitter (PBS). Birefringent wave-plates are optical components where the refractive index is different along two perpendicular axes. Orthogonal polarizations obtain different phase as they travel through the media, and the wave-plate can therefore transform between polarization states. In a half-wave plate (HWP), the relative phase shift of the two axes is $\frac{\pi}{2}$. By rotating the HWP by an angle Θ between its fast axis and the horizontal component of polarization, it can transform between all linear polarization states

$$\begin{aligned} HWP(\Theta)|H\rangle &= \cos 2\Theta|H\rangle + \sin 2\Theta|V\rangle \\ HWP(\Theta)|V\rangle &= \sin 2\Theta|H\rangle - \cos 2\Theta|V\rangle. \end{aligned} \tag{2.15}$$

As a PBS is an optical component that transmits $|H\rangle$ states and reflects $|V\rangle$ states, a photon detector in the reflected and transmitted arm can be associated with a measurement in the

H/V basis. By inserting a HWP in front, we can rotate the measurement basis between all linear polarization states. Similarly, a quarter wave-plate (QWP) can be used to obtain circular polarizations.

2.2.2 Spectral and Temporal Modes

In contrast to polarization, the spectral/temporal modes of the photon inhabit an infinite-dimensional Hilbert space. Exploiting this is a natural goal of QIS, as it allows one to extend the qubit state to d-dimensional *qudit* states, able to contain $\log_2 d$ bits of information. As frequency and time are conjugate variables related through the Fourier transform, we might interchangeably talk about spectral and temporal modes (TMs) of the photon.

An artifact of the free field expansion we started with (Eq. 2.1) is that the basis choice resulted in modes with definite frequency. This is only possible due to the completely delocalized nature of the space-time coordinates of plane waves, which does little to elucidate the rich structure of temporal modes the photon may inhabit. In the more general picture, the photon must be localized within some time and space in our experimental setup. This can be realized by representing the spectral/temporal states as superpositions over monochromatic states $\{|\omega_1\rangle, |\omega_2\rangle, |\omega_3\rangle, ...\}$ with some arbitrary weighting function $f_j(\omega)$

$$|\psi_j\rangle^{TM} = \frac{1}{2\pi}\int d\omega f_j(\omega)\hat{a}^\dagger(\omega)\,|0\rangle\,, \tag{2.16}$$

requiring only that the weighting function is normalized. Equivalently, we can represent this as superpositions over states $\{|t_1\rangle, |t_2\rangle, |t_3\rangle, ...\}$, indicating the presence of a photon at time t_i

$$|\psi_j\rangle^{TM} = \int dt \tilde{f}_j(t)\hat{a}^\dagger(t)\,|0\rangle\,, \tag{2.17}$$

where the corresponding weighting function $\tilde{f}_j(t)$ is the Fourier transform of $f_j(\omega)$. Encoding information in orthogonal TM states, for example by a basis of Hermite-Gaussian weighting functions, is a concept that only in recent years have gained traction [27, 28]. The idea is however intriguing, as a large set of TMs may be distributed in a single spatial mode, thus proving very suitable for use in single-mode optical fibers. In contrast to polarization however, manipulation of TMs are difficult, and require the use of nonlinear optics phenomena such as three-wave mixing [29]. Therefore, it is likely still a way to go until this formalism is mature.

In this thesis, we will rather investigate a scheme called *time-bin* encoding. These type of protocols typically utilize an unbalanced Mach-Zehnder interferometer to split a single

temporal mode into a superposition of both interferometer paths, which we may denote by short $|S\rangle$ and long $|L\rangle$

$$|\psi\rangle_{\mathrm{time-bin}} = |S\rangle + e^{i\phi}\,|L\rangle\,. \tag{2.18}$$

The quantum information is then encoded in the relative time-of-arrival of the photon, which due to the digital nature of data acquisition must be split into discrete time-bins. This type of encoding is especially appealing in entanglement based setups, where the intrinsic time correlations between two entangled photons can be used to expand the time-bin state into higher dimensional qudits. The Franson interferometer realizes exactly such a scheme, and is discussed in more detail in Section 3.4.

2.2.3 Spatial and Momentum Modes

The spatial modes of the photon, related to the momenta through the spatial Fourier transform, sums up the last possibility for information encoding in single-photon states. I mention them here only for completeness, as they will not be relevant for this thesis. This DOF draws many parallels to the temporal modes, in that a basis choice of Hermite-Gaussians or Laguerre-Gaussians reveal a rich structure of orthonormal field modes, which we refer to as the orbital angular momenta (OAM) of the photon. Encoding information in the OAM of photons has received considerable interest in the later years [30], as they too inhabit an in principle infinite-dimensional Hilbert space. Furthermore, it can be manipulated with stationary optical elements, such as spatial light modulators. Some drawbacks of this encoding is that they cannot be implemented with single-mode optical fibers and it is susceptible to turbulence in free-space links.

2.3 Quantum Entanglement in Two-Photon Systems

A central feature of this thesis is the concept of quantum entanglement in pairs of photons. In a general sense, a two-photon state is said to be entangled when the composite state cannot be factorized into a tensor product of the two individual photon states, A and B

$$|\Psi\rangle_{AB} \neq |\Psi\rangle_A \otimes |\Psi\rangle_B. \tag{2.19}$$

Consequently, the two-photon state must be considered as a whole, regardless of the physical separation between the individual photons. As such, quantum entanglement represents a phenomena that thoroughly challenges our intuitive picture of the world, and that sparked

one of histories most famous scientific debates. To see why, I first introduce the four maximally entangled Bell states

$$|\Psi^{\pm}\rangle = \frac{1}{\sqrt{2}}(|H\rangle_A |V\rangle_B \pm |V\rangle_A |H\rangle_B), \tag{2.20}$$

$$|\Phi^{\pm}\rangle = \frac{1}{\sqrt{2}}(|H\rangle_A |H\rangle_B \pm |V\rangle_A |V\rangle_B). \tag{2.21}$$

The Bell states are maximally entangled in the sense that a measurement on photon A unequivocally determines the polarization of photon B. The expected outcome of any measurement on the individual photons however is completely random. Information lies in the perfect correlation between the states. Classically, it is easy to imagine a similar state occurring from our incomplete knowledge of the system. A statistical mixture of the two product states $|H\rangle_A |V\rangle_B$ and $|V\rangle_A |H\rangle_B$ would evidently give the same results, thus simply reflecting our incomplete knowledge of the initial state of the system. The conclusive difference from the correlations found in quantum entangled systems first become evident when we change between the measurement bases. More generally, as shown by the CHSH-version of the famous Bell inequality [31], classical correlations in the presence of two different bases choices of the measurement operators $(\hat{\sigma}^A_{\mathbf{a}}, \hat{\sigma}^B_{\mathbf{b}})$ and $(\hat{\sigma}^A_{\mathbf{a}'}, \hat{\sigma}^B_{\mathbf{b}'})$ must always yield correlations bounded by

$$|\langle S\rangle| = |E(\mathbf{a},\mathbf{b}) - E(\mathbf{a},\mathbf{b}') + E(\mathbf{a}',\mathbf{b}) + E(\mathbf{a}',\mathbf{b}')| \leq 2, \tag{2.22}$$

where we used the notation $E(\mathbf{a},\mathbf{b}) = \langle \hat{\sigma}^A_{\mathbf{a}} \hat{\sigma}^B_{\mathbf{b}} \rangle$. The fundamental assumptions in the derivation of this inequality is that our universe exhibits two concepts known as *locality* — that interactions are limited by the speed of light — and *realism* — that it is possible to assign properties to a particle independent of our observation. However, using the quantum mechanical formalism for polarization measurements, restricting for simplicity the measurement basis to the plane of linear polarizations on the Bloch sphere, the directions $\mathbf{a}, \mathbf{b}, \mathbf{a}', \mathbf{b}'$ can be identified with angles $\alpha, \beta, \alpha', \beta'$, which for the values $\alpha = 0°$, $\beta = 22.5°$, $\alpha' = 45°$, $\beta' = 67.5°$ violates the inequality with a maximum value of $|\langle S\rangle| = 2\sqrt{2}$.

The paradox is now apparent. As far as we know, there is no fundamental force mediating any photon-photon interaction. Furthermore, the assumptions of relativity is that the speed of any such force is limited by the speed of light. Yet, changing the measurement basis of one photon, somehow affects the outcome of a measurement on its entangled partner in a way that cannot be reconciled with locality and/or realism. This apparent impossibility was also the famous position of Einstein [32], which used it as an argument for the incompleteness of quantum mechanics — notably, 29 years in advance of Bell's famous inequality [2], and 37 years before the first experimental tests by Freedman and Clauser [4] verifying the violation. To date, quantum entanglement has been consistently verified in a plethora of experiments, using the entire spectra of photon degrees of freedom,

ranging from polarization [3–8], momentum [10, 11], energy-time [9] and even with the simultaneous entanglement in all of them [12].

Loopholes A common issue in verifying Bell inequalities is that of getting rid of loopholes in the experimental assumptions. Some known loopholes are the *fair sampling loophole* — regarding the assumption that the subset of photons that are detected are representative for the entire ensemble — the *freedom-of-choice loophole* — that the experimenter is truly free to make random basis choices — and the *locality loophole* — that the two detection events are causally disconnected in the space-time metric. Numerous experiments have gone to great lengths to limit the plausibility of such loopholes [e.g. 6, 7, 13, 33], and as so I will not pay any considerable interest in them for the rest of this thesis.

Entanglement Witnesses Violating Bell inequalities is only necessary to prove the inconsistency of quantum mechanics with localism and/or realism. However, assuming the validity of quantum mechanics, this imposes an unnecessary strict criteria if the only goal is to verify entanglement, in which it is only necessary to be able to distinguish the entangled state from a mixed state. For the two-photon polarization entangled state, a sufficient condition is that the entanglement witness $\mathcal{W}$ is negative

$$\mathcal{W} = \frac{1}{2} - \frac{1}{4}(1 + V_{H/V} + V_{D/A} + V_{L/R}), \tag{2.23}$$

where $V_{H/V}$, $V_{D/A}$ and $V_{L/R}$ denotes the entanglement visibility in the H/V, D/A and L/R bases. The visibility here is an experimental quantity, that denotes the contrast between the measured polarization coincidences in each basis. For a $|\Phi^+\rangle$ state, this quantity is expressed as

$$V_{H/V} = \frac{CC_{HH} + CC_{VV} - CC_{HV} - CC_{VH}}{CC_{HH} + CC_{VV} + CC_{HV} + CC_{VH}}, \tag{2.24}$$

where the *coincidence count*, CC_{ij}, is the number of simultaneous photon detection events with polarizations $i, j \in \{H, V\}$, and similarly for the other bases. It is clear that an average visibility of 33% in each basis is necessary to verify entanglement. Experimentally, it is usually more convenient measuring the visibility in two bases only, posing the somewhat stricter requirement of 50% average visibility. In general, constructing entanglement witnesses is a challenge that will vary with the specific entangled state one considers. For a thorough discussion on the issue I refer to [34].

Relevance to Quantum Information Science Entanglement has during the last decades been verified in numerous experiments, and while the initial motivation has been from a fundamental physics standpoint, it has gradually become apparent that entanglement holds great technological promise. Within QIS, it has found applications in hot research topics such as quantum computing [35], teleportation [36] and quantum key distribution [37]. For our purposes, I will describe an experiment (Chapter 5) where entanglement is used

as a resource for a quantum key distribution protocol, and we will look at states entangled in both polarization and time-bins simultaneously — so-called *hyperentanglement*. This principle is quite straightforward, as the two degrees of freedom simply factor out into separate entangled states, e.g.

$$\begin{aligned} |\Psi\rangle =& |\Psi^+\rangle_{pol.} \otimes |\Psi^+\rangle_{time-bin} \\ =& \frac{1}{2}(|H\rangle_A |V\rangle_B + |V\rangle_A |H\rangle_B) \otimes (|t_1\rangle_A |t_2\rangle_B + |t_2\rangle_A |t_1\rangle_B) \end{aligned} \tag{2.25}$$

In the scheme we explore in Chapter 5, the polarization DOF will act as an ancilla for the time-bin DOF, increasing the noise robustness and information capacity of the QKD channel.

Chapter 3

Toolbox for Two-Photon Entanglement Experiments

In this chapter I present conventional experimental tools for producing and verifying entanglement in pairs of photons. First, I describe the theoretical framework of the spontaneous parametric down-conversion (SPDC) process, known to produce states of entangled photon pairs in all degrees of freedom. To produce co-propagating polarization entangled pairs, this is usually implemented in a Sagnac loop configuration, which I explain next. The remainder of the chapter is dedicated to interferometric designs that can verify the presence of polarization entanglement and energy-time entanglement.

3.1 Producing Entangled Photon Pairs

Developing stable and efficient sources for photon entanglement is an important step for the maturity of QKD. The arguably most popular technique to date is the process of spontaneous parametric down-conversion, which is also the source of use in this thesis.

3.1.1 Spontaneous Parametric Down-Conversion

In the SPDC process, a single *pump* photon is down-converted into two photons of lower energy, conventionally called *signal* and *idler* photons. The process is strictly a quantum mechanical phenomena, as the effect arise from the spontaneous interaction of the pump

photon with the signal and idler vacuum fields. This is made possible by the nonlinear polarization response of certain crystals, such as beta barium borate (BBO), potassium titanyl phosphate (KTP) and lithium niobate (LN) to name a few. The polarization of crystals describes the behaviour of its internal dipoles to an external electrical field. For crystals where third and higher order contributions are negligible, the nonlinear part of the polarization vector $\mathbf{P}$ can be written

$$P_i^{NL}(\mathbf{r},t) = \int dt_1 dt_2 \chi_{ijk}^{(2)}(\mathbf{r}, t-t_1, t-t_2) E_j(\mathbf{r},t_1) E_k(\mathbf{r},t_2) + O(\mathbf{E}^3), \tag{3.1}$$

where χ is known as the susceptibility, or response function, of the material. As the relevant interaction describes the creation and annihilation of photons, we must use the field operator formalism to derive the SPDC two-photon state. We find the relevant terms by considering the Hamiltonian of the electromagnetic field in a non-magnetic, but dielectric medium [20]

$$H_{EM} \propto \int \mathrm{d}^3\mathbf{r}\mathbf{E}(\mathbf{r},\mathrm{t}) \cdot \mathbf{D}(\mathbf{r},\mathrm{t}), \tag{3.2}$$

where $\mathbf{D}(\mathbf{r},t) = \epsilon_0 \mathbf{E}(\mathbf{r},t) + \mathbf{P}(\mathbf{r},t)$. We can here use the field operators introduced in Eq. 2.1, only altering the relationship $|\mathbf{k}| = n(\omega)\omega/c$, where $n(\omega)$ is the refractive index of the crystal. This expression now describes all possible second order non-linear interactions in the crystal. We're only interested in the interaction where one pump photon is down-converted into a signal and idler photon, and are therefore left with the SPDC Hamiltonian

$$\hat{\mathbf{H}}_{SPDC} \propto \int d^3\mathbf{r} \hat{\mathbf{E}}_p^- \hat{\mathbf{E}}_s^+ \hat{\mathbf{E}}_i^+. \tag{3.3}$$

The SPDC process can be categorized into type-0, type-1 and type-2, according to the relation of the polarization between the pump, signal and idler photons, as illustrated in Fig. 3.1. To obtain the resulting state of any of these is a matter of time evolving the initial state, consisting of the pump field and the signal and idler vacuum fields, with some assumptions on the geometry of the system. This derivation is rather lengthy, and is described in detail in a number of sources [e.g. 20, 38–40]. For a type-2 process, where the signal and idler occupy orthogonal polarization states, the SPDC state takes the form

$$|\Psi\rangle_{SPDC} \propto \int d\omega_s d\omega_i \Phi(\mathbf{k}_s^\perp, \mathbf{k}_i^\perp, \omega_s, \omega_i) \left|\mathbf{k}_s^\perp, \omega_s, V_s\right\rangle \left|\mathbf{k}_i^\perp, \omega_i, H_i\right\rangle, \tag{3.4}$$

where $\Phi(\mathbf{k}_s^\perp, \mathbf{k}_i^\perp, \omega_s, \omega_i)$ is the joint-spectral amplitude

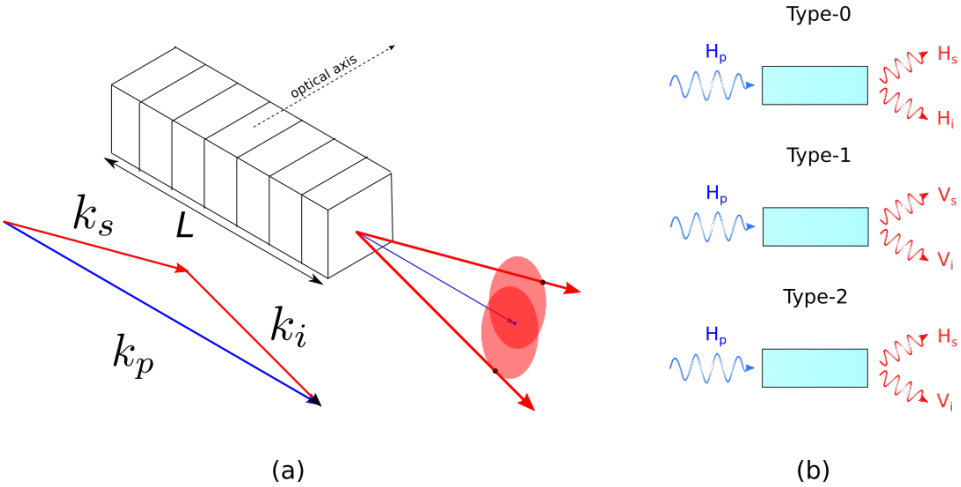

Figure 3.1: (a) Illustration of a typical crystal geometry. The complex phase-matching conditions define a set of emission cones assigned to the signal and idler photons. The conservation of transverse momenta restricts the emission of the signal and idler photons along conjugate points on their respective cones. (b) The SPDC process can be categorized into three types according to the relation between the polarization of the incident pump photon to the polarization of the signal and idler photons.

$$\Phi(\mathbf{k}_s^\perp, \mathbf{k}_i^\perp, \omega_s, \omega_i) \propto E_p(\mathbf{k}_s^\perp + \mathbf{k}_i^\perp)\alpha_p(\omega_s + \omega_i)\,\mathrm{sinc}(\Delta k^z L/2). \tag{3.5}$$

The distribution of transverse momenta of the pump field $E_p(\mathbf{k}_p^\perp) = E_p(\mathbf{k}_s^\perp + \mathbf{k}_i^\perp)$, ensures the conservation of transverse momenta along emission cones for the signal and idler modes, while the spectral distribution $\alpha_p(\omega_p) = \alpha_p(\omega_s + \omega_i)$ ensures energy conservation. The final term is known as the phase-matching condition, and ultimately controls the emission probabilities of each $|\mathbf{k}_s^\perp, \omega_s, V_s\rangle\,|\mathbf{k}_i^\perp, \omega_i, H_i\rangle$ state. Maximal efficiency requires that $\Delta k^z = 0$, where

$$\Delta k^z = k_p^z(\omega_i + \omega_s, \mathbf{k}_i^\perp + \mathbf{k}_s^\perp) - k_i^z(\omega_i, \mathbf{k}_i^\perp) - k_s^z(\omega_s, \mathbf{k}_s^\perp). \tag{3.6}$$

However, nonlinear crystals typically suffer from chromatic dispersion, meaning that the refractive index is dependent on the frequency of the photon modes. Consequently, the phase-matching condition is not easily realized under the condition of energy conservation, which we can see from rewriting the phase-matching requirement

$$\frac{n(\omega_p)\omega_p}{c} = \frac{n(\omega_i)\omega_i}{c} + \frac{n(\omega_s)\omega_s}{c}. \tag{3.7}$$

For type-1 and type-2 sources, this can be solved by utilizing the birefringence of the crystals. By adjusting the angle of the optical axis of the crystal in respect to the pump, signal and idler field, one can engineer the dispersion of the different frequencies to be cancelled out by the dispersion of different polarizations caused by the birefringence. This results in certain emission cones for the signal and idler photons, where the SPDC process is phase-matched (see Fig. 3.1). A more common technique today is the periodic poling of the electric susceptibility tensor $\chi^{(2)}$. By engineering the nonlinear crystal such that the sign of the susceptibility switches with a certain period $\frac{2\pi}{\Lambda}$, the phase-matching condition takes the form

$$\Delta k^z = k_p^z(\omega_i + \omega_s, \mathbf{k}_i^\perp + \mathbf{k}_s^\perp) - k_i^z(\omega_i, \mathbf{k}_i^\perp) - k_s^z(\omega_s, \mathbf{k}_s^\perp) - \frac{2\pi}{\Lambda}. \tag{3.8}$$

By carefully adjusting the poling period, one can design crystals that allow efficient down-conversion for specific operational temperatures and emission angles. This is known as *quasi-phase-matching*, and is typically utilized in Sagnac configurations, where it is necessary to use crystals that allow co-propagating signal and idler modes.

3.1.2 Entanglement from SPDC

In principle, it is possible to obtain entanglement in all degrees of freedom from the SPDC process. For momentum and polarization modes however, this require superpositions of certain emission events along the signal and idler cones (see e.g. [41]), and is not necessarily realized when the crystal is engineered for co-propagating modes. Energy-time entanglement on the other hand is intrinsic to the process. This is straight forward to see, as the joint-spectral amplitude $\Phi(\mathbf{k}_s^\perp, \mathbf{k}_i^\perp, \omega_s, \omega_i)$ makes it impossible to factorize the two-photon state into separate Hilbert spaces. The nature of energy entanglement can be thought of from the perspective that the signal and idler photons initially have uncertain frequencies due to the many ways of dividing the pump frequency. However, since the sum of the two frequencies must add up to the pump frequency, measuring the energy of one photon instantaneously determines the energy of its partner.

The temporal shape of the SPDC function can be derived by assuming a shape of the spectral distribution of the pump field. All SPDC sources in this thesis use continuous-wave (cw) pump lasers that can be approximated as nearly monochromatic modes such that $\alpha_p(\omega_i + \omega_s) \approx \delta(\omega_i + \omega_s)$. It is then convenient to introduce the frequency deviation from the pump frequency $\Omega = \omega_s - \omega_p \ (= \omega_p - \omega_i)$, in order to rewrite the SPDC state (omitting spatial and polarization terms)

$$|\Psi^{cw}\rangle \propto \int d\Omega \Phi(\Omega) \, |\Omega\rangle_s \, |-\Omega\rangle_i \, . \tag{3.9}$$

Using the formalism of Section 2.2.2, we can then define temporal wave-packets for the signal and idler modes [24, 39]

$$A^{\dagger}(T) = \frac{1}{\sqrt{2\pi}} \int d\Omega \sqrt{\Phi(\Omega)} e^{i(\omega_p/2+\Omega)T} a^{\dagger}(\omega_p/2 + \Omega), \tag{3.10}$$

which yields the cw-SPDC state in terms of temporal wave-packets

$$|\Psi^{cw}\rangle \propto \int dT e^{-i\omega_p T} |T\rangle_s |T\rangle_i . \tag{3.11}$$

The physical picture of energy-time entanglement in the SPDC process may then equivalently be considered as a large uncertainty in the creation time of the signal and idler modes, essentially limited by the coherence time of the pump field, which collapses once one of the photons are detected. As the two photons are created simultaneously, a detection of one entangled photon should always lead to a so-called *coincidence detection* of the other. The efficiency in which photon detection events lead to coincidence detection will generally depend on the experimental setup however, as less than unity coupling efficiency and detector sensitivity leads to loss of coincidence events.

3.2 The Sagnac Source

As polarization entanglement does not appear from the SPDC process in the case of co-propagating signal and idler modes, most modern experimental setups use the Sagnac configuration to overcome this. The principle of this source design relies on the indistinguishable superposition of two SPDC modes. The maximally entangled Bell state

$$|\Psi^{+}\rangle = \frac{1}{\sqrt{2}}(|H_s, V_i\rangle + e^{i\Phi} |V_s, H_i\rangle), \tag{3.12}$$

may for example be realized by superimposing two SPDC modes, $|H_s, V_i\rangle$ and $|V_s, H_i\rangle$, created in a type-2 process. However, this requires that the joint-spectral amplitudes, $\Phi_{H_s V_i}$ and $\Phi_{V_s H_i}$, of each SPDC pair are identical, as only then the spectral amplitudes can be factorized out to give the entangled state. Although this can be done in several ways, e.g. with a crossed crystal configuration [38], the Sagnac loop is particularly appealing as it achieves the matching of the joint-spectral amplitudes from the intrinsic symmetry of its setup, which is illustrated in Fig 3.2. Furthermore, the Sagnac source has the advantage of a rather high conversion efficiency [38, 42, 43].

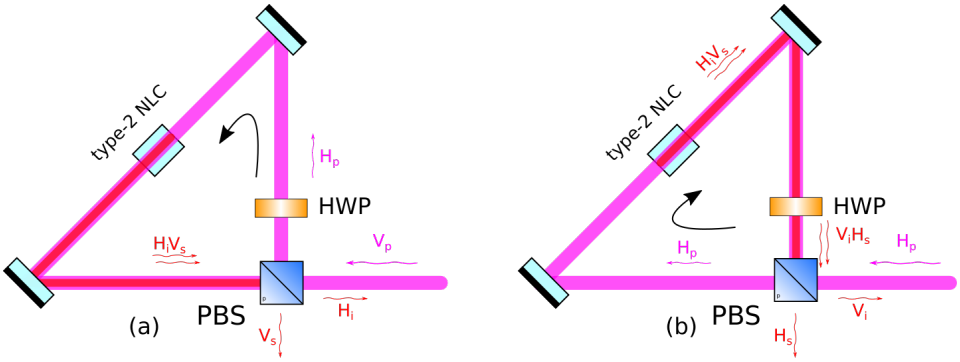

Figure 3.2: A type-2 nonlinear crystal (NLC) is pumped in the counter-clockwise (a) and clockwise (b) loop directions by splitting the diagonally polarized pump beam with a polarizing beam splitter (PBS). See the text for further explanation.

In the Sagnac configuration, a diagonally polarized pump photon $|D\rangle$ is directed towards a PBS. The pump photon is therefore split into a superposition of its horizontal and vertical component, travelling the loop in opposite directions. The horizontal component is transmitted, propagating clockwise through the loop, while the vertical component is reflected into the counter-clockwise direction. A half-wave plate oriented at $45°$ flips the vertical component to horizontal, such that both components are horizontally polarized when they pump the crystal. The SPDC interaction in a type-2 nonlinear crystal then creates the $\Phi_{HV}\,|H_s\rangle\,|V_i\rangle$ two photon state, with identical joint-spectral amplitudes for both pump directions. The clockwise oriented photon pair then passes the half-wave plate, flipping the polarizations of the signal and idler photon. After traversing the PBS once more, each two-photon state is split up, such that the two components $|H_iV_s\rangle$ and $|V_iH_s\rangle$ of the now maximally entangled Bell state exit the PBS in separate spatial modes. At this point, it is worth mentioning that the process is completely identical for type-0 and type-1 sources, with the only exception that the entangled pair will exit in the same spatial mode, meaning that non-degenerate frequency modes usually must be used to decouple the photons, e.g. with a dichroic mirror.

Finally, an additional advantage of the Sagnac setup is the ease of which the phase Φ between the two-photon states can be tuned, as it simply is a sum of the pump phase ϕ_p and the passive contribution from dispersion in the PBS.

3.3 Polarization Analyzing Module

A polarization analyzing module is a photon detection module able to verify a polarization entangled state. This is commonly referred to as a *Alice-module* and/or *Bob-module* due to its frequent use in QKD setups, where communication takes place between two hypothetical parties named Alice and Bob. An entanglement witness for polarization entanglement

was already presented in Eq. 2.23, which relies on basis measurements in the three H/V, D/A and L/R MUBs. As it rarely poses an issue to obtain high polarization visibilities, it is slightly easier to implement measurements in the H/V and D/A bases only, yielding the witness

$$\mathcal{W} = \frac{1}{2} - \frac{V_{H/V} + V_{D/A}}{2}. \tag{3.13}$$

Consequently the average visibility in the two bases must exceed 50 % to verify entanglement. An implementation of the necessary setup to perform these measurements is illustrated in Fig. 3.3. It begins with a 50-50 beam splitter (BS), working as a passive distributor between the two measurement bases. The transmitted arm goes to a PBS, where horizontally polarized photons are transmitted and vertically polarized photons reflected, thus working as a projection operation in the H/V basis. In the reflected arm of the BS, a half-wave plate set at $22.5°$ first shifts the polarization to the D/A basis, subsequently impinging the photons on a PBS in the H/V basis. The operation of the HWP together with the PBS is equivalent to a measurement operation in the D/A basis. In order to measure the visibilities of entangled polarization states, the coincidence counts between each single-photon counting module (SPCM) in the two separate modules must be compared (see Eq. 2.24).

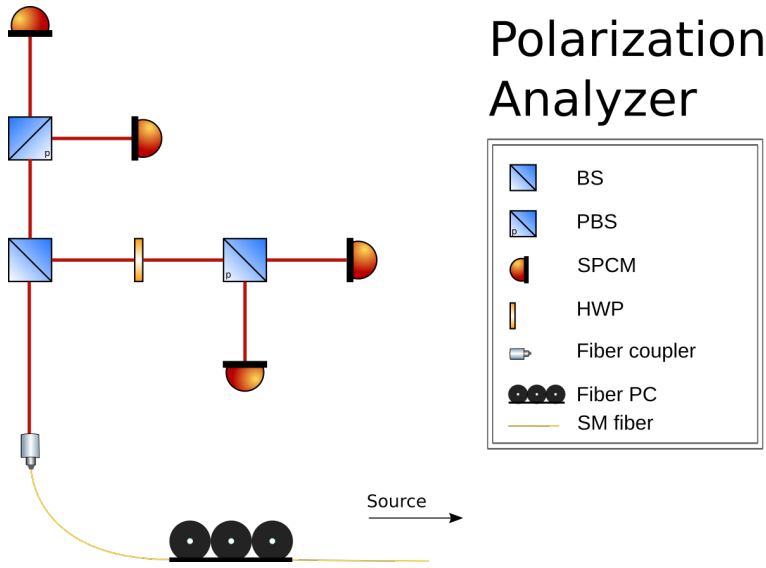

Figure 3.3: Illustration of a typical setup for a polarization analyzing module, measuring photon polarizations in the H/V and D/A bases. A single-mode (SM) fiber and an in-fiber polarization controller (PC) are typically used in the connection from the source to the module. The setup is further explained in the text.

3.4 The Franson Interferometer

The Franson interferometer, suggested by J.D. Franson in 1989 [44], provides a way of verifying energy-time entanglement in photon pairs. I will here first present the original idea by Franson, before I in Section 3.4.1 discuss a modified setup without some of the post-selection issues the original experiment contains.

Franson originally envisioned a three-level atomic system with an initially long decay time τ_1 and subsequently a much shorter decay time τ_2. The two photons are thus highly correlated in time, as the detection of one photon causes the initially large uncertainty in detection time of the other photon to collapse. The same argument applies for the SPDC entangled state, which we for consistency will consider in this derivation. The setup Franson devised, Fig. 3.4, consists of two equally unbalanced Mach-Zehnder interferometers, with long and short arms L_i, S_i and locally variable phase shifts ϕ_1, ϕ_2. The path length difference $\Delta L = L_i - S_i$ must be long enough to rule out single-photon interference in each Mach-Zehnder interferometer, i.e. longer than the signal and idler coherence length, $l_c^{i,s}$, while being shorter than the coherence length of the pump beam, l_c^p, such that interference in the coincidence counts between the two interferometers are possible

$$l_c^{i,s} \leq \Delta L \leq l_c^p. \tag{3.14}$$

The study of coherence is a large topic in its own right, and I refer to [e.g. 17, 43, 45, 46] for a more in depth discussion. For our purposes it is enough to state that the coherence time usually is inversely proportional to the bandwidth of the spectral mode of the state, $\tau_c \propto 1/\Delta\omega$. For the signal and idler photons, this is dependent on the shape of the joint-spectral amplitude, which yields a broader bandwidth than the nearly monochromatic pump laser, and thus shorter coherence time, satisfying the criteria for Franson interference.

The non-local interference properties of the Franson interferometer arise from the superposition of possible photon paths, that interfere within the coherence time of the pump laser. Let $|\psi(\mathbf{r}_i, t)\rangle$ denote the state of each photon wave-packet at position $\mathbf{r}_i$, corresponding to one of the four detectors $i \in \{D_1, D_1', D_2, D_2'\}$. This superposition can for each photon be expressed as a sum of the two possible photon paths

$$|\psi(\mathbf{r}_i, t)\rangle = \frac{1}{\sqrt{2}}(|S_i\rangle + e^{i\phi_i}|L_i\rangle), \tag{3.15}$$

where ϕ_i is the local phase shift applied along the long arm. As the state $|L_i\rangle$ is simply a time evolution of the incident field, the two states are related through

$$|L_i\rangle = e^{i\phi_i} e^{i\omega\Delta T}|S_i\rangle, \tag{3.16}$$

where the phase shift $\Delta\Phi = \omega\Delta T$, with $\Delta T = \Delta L/c$, is the phase shift from the freely propagated field along ΔL.

The coincidence rate between detectors at position i, j is then given from calculating the expression

$$R^c_{i,j} = \langle \psi(\mathbf{r}_i, t)\psi(\mathbf{r}_j, t)|\psi(\mathbf{r}_i, t)\psi(\mathbf{r}_j, t)\rangle \,. \tag{3.17}$$

Writing out this equation gives rise to four separate terms, corresponding to the four different path combinations of the signal and idler photons, which we can denote as $|S_s, S_i\rangle$, $|S_s, L_i\rangle$, $|L_s, S_i\rangle$ and $|L_s, L_i\rangle$. The two terms with different paths do not give rise to interference, as the detection events are distinguishable in their arrival time. The two remaining terms are indistinguishable since the coherence time of the pump is larger than ΔT. This result in a coincidence rate between detectors D_1 and D_2 of the form [44]

$$R^{1,2}_c = \frac{1}{4}\cos^2\left(\frac{\phi_1 + \phi_2 + \omega_p \Delta T}{2}\right), \tag{3.18}$$

Noticeably, this is the same $\cos^2$-form of the coincidence rates one obtains for polarization entangled states when rotating the measurement basis (see Section 4.5.2). However, the original Franson interferometer has a serious setback in terms of using it as a test of Bell's inequality. Mainly, this has to do with the non-interfering background of 50 % of the photon detection events due to the $|S_s, L_i\rangle, |L_s, S_i\rangle$ paths. This creates a loophole for which local hidden-variable theories can be created [e.g. 47, 48].

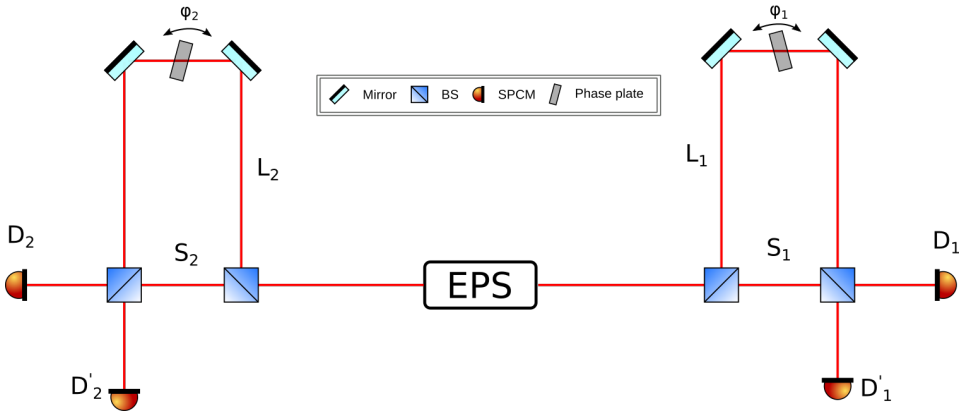

Figure 3.4: Illustration of a Franson interferometer. An entangled photon source (EPS) passes photons to separate unbalanced Mach-Zehnder interferometers. The path length difference in each interferometer is such that single-photon interference is impossible, while shorter than the coherence length of the pump laser. A local phase shift can be adjusted in each interferometer, showing that the local measurement settings of each observer affect the coincidence rates in a non-local way.

3.4.1 The Post-Selection Free Franson Interferometer

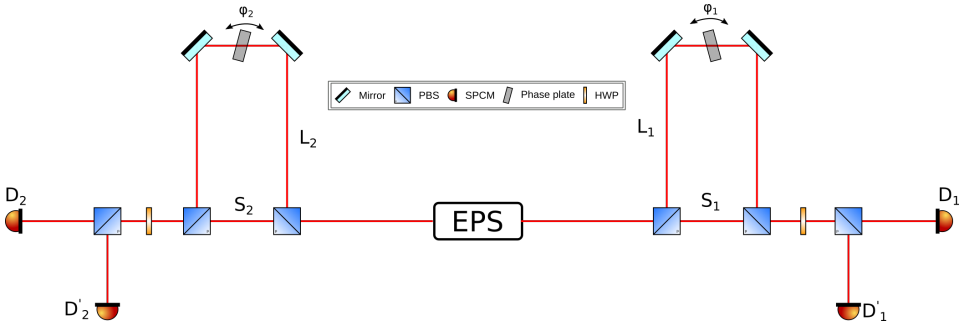

Figure 3.5: The post-selection free Franson interferometer uses polarizing beam splitters and polarization entanglement as an ancilla to remove the non-interfering background of the original setup. Which-path information is then destroyed by measuring the polarization in a mutually unbiased basis, restoring interference.

In order to get rid of the non-interfering background in the original Franson setup, the post-selection free Franson interferometer (see Fig. 3.5) utilizes the idea of destroying which-path information by measuring polarization in mutually unbiased bases [43, 49, 50]. This is done with the help of a hyperentangled state

$$|\Psi\rangle \propto \frac{1}{\sqrt{2}}(|H_i H_s\rangle + |V_i V_s\rangle) \otimes \int dT e^{-i\omega_p T} |T\rangle_s |T\rangle_i . \tag{3.19}$$

Due to the nature of the entangled polarization state and the polarizing beam splitters, the signal and idler photon will now either both take the short path or both the long path, such that the events with distinguishable arrival time simply does not exist anymore. The state after the unbalanced Mach-Zehnder interferometers can then be written as

$$|\Psi\rangle \propto |H_i S_i\rangle |H_s S_s\rangle + e^{i\Phi} |V_i L_i\rangle |V_s L_s\rangle , \tag{3.20}$$

where the extra phase shift as before corresponds to the free field propagation along the long paths, in addition to the local phase shifts ϕ_1 and ϕ_2

$$\Phi = (\omega_p/2 + \Omega)\Delta T + (\omega_p/2 - \Omega)\Delta T + \phi_1 + \phi_2 = \omega_p \Delta T + \phi_1 + \phi_2. \tag{3.21}$$

The two different paths are however not anymore indistinguishable, as the polarization of each photon labels the path taken, and any interference can therefore not arise from this state. However, as mentioned before, which-path information can be destroyed by measuring in mutually unbiased bases. In the post-selection free Franson interferometer, we can do this by first transforming the polarization by a half-wave plate oriented at $22.5°$ with respect to the horizontal axis, such that $|H\rangle \rightarrow |D\rangle$ and $|V\rangle \rightarrow |A\rangle$

$$HWP(22.5^\circ)\left|\Psi\right\rangle = \left|D_i S_i\right\rangle \left|D_s S_s\right\rangle + e^{i\Phi}\left|A_i L_i\right\rangle \left|A_s L_s\right\rangle, \tag{3.22}$$

before the state is projected onto its horizontal and vertical components by a PBS. The coincidence rate between D_1 and D_2 corresponds to a measurement of two horizontally polarized photons, which returns the same coincidence rate as before

$$R^c_{1,2} = \left|\left\langle H_i H_s|\Psi\right\rangle\right|^2 = \frac{1}{4}\cos^2\left(\frac{\phi_1 + \phi_2 + \omega_p \Delta T}{2}\right). \tag{3.23}$$

Chapter 4

Feasibility of Measuring Time Dilation with the Two-Photon Coincidence Peak

Photon pairs produced in SPDC sources exhibit temporal correlations in their detection times within $1\,\mathrm{ps}$. This offer the attractive possibility of using the detection times of entangled photon pairs for time synchronization between remote locations. Utilizing time-correlated SPDC pairs for remote clock synchronization is not a new idea, and has for exampled been explored in [51–54]. The motivation behind this chapter is rather to investigate the same principle as a tool for time and frequency metrology. This becomes especially interesting as we already are at an era where QKD is being launched into space (see e.g. [55–59]). At these scales, it is feasible that time dilation effects enters the region of timing resolutions in modern QKD setups. To explore this topic, I first provide a brief introduction into the concept of gravitational time dilation and timing standards, before the principle of using entangled photons for remote clock synchronization is discussed. The setup we use for this experiment also provided a nice opportunity to test the theoretical predictions on polarization entanglement, which is why I include a section on the violation of Bell's inequality. Finally, a series of results from the clock synchronization test is presented, which we use to discuss the concept as a tool within metrology on a larger scale.

4.1 Background: Time Dilation and Timing Standards

The gravitational potential of earth cause clocks at different height in the potential field to tick at different rates, an effect known as gravitational time dilation. For small height differences near earth's surface, the effect can be derived in the weak-field limit, giving the expression [60]

$$\frac{\delta f}{f_0} = \frac{g\Delta h}{c^2}, \tag{4.1}$$

for the fractional frequency shift $\delta f/f_0 = (f_1 - f_0)/f_0$ of two clocks separated by a height Δh, with c being the speed of light and g the gravitational acceleration at earth's surface. This corresponds to a fractional frequency shift of 1.1×10^{-16} per meter of height difference. Such minuscule frequency differences makes the effect experimentally challenging to verify, requiring extremely accurate time standards.

A time standard is simply an oscillator able to produce a reference frequency, joined by a counting mechanism, and can be anything from a normal pocket watch to a modern atomic clock. Developing accurate time standards is an important research topic in its own right, and one that has seen tremendous advances over the last century. Time accuracies comparable to the effects of time dilation was first possible to produce with the invention of the atomic clock in the 1950s, the fundamental principle of which is to stabilize the frequency of a laser, with *hyperfine* transition lines in atoms as highly accurate reference frequencies.

Two key parameters in the characterization of clocks is the accuracy and the stability. Whereas accuracy refers to the closeness of the clock frequency to the predicted frequency of the transition line, stability refers to the variation in clock frequency over time. Although both have complex characteristics, they are intrinsically dependent on the frequency and linewidth of the transition, which together determine the relative uncertainty in the reference frequency. A straightforward way of reducing this uncertainty is to increase the frequency of the transition line, which is why clocks based on hyperfine transitions in the visible frequency ranges, so-called *optical clocks*, are the next research step in the continued improvement in timing standards.

The development of highly accurate atomic clocks made possible the famous Hafele-Keating experiment in 1972 [61], where the predicted time dilation effects of both special and general relativity was verified by comparing cesium based atomic clocks flown on round trips around the earth, with identical clocks located at ground. The perhaps most impressive measurement of gravitational time dilation to date was performed by researchers at NIST [60], where they developed two optical clocks based on transition lines in $^{27}\mathrm{Al}^{+}$ ions. With frequency uncertainties below 10^{-16} — that is, an expected error of one second every 10 quadrillion years — they managed to resolve the time dilation effect on a height difference of $33\,\mathrm{cm}$.

4.2 Assessing Clock Stability

Assessing the stability of different frequency standards is not a straightforward issue, lending to the fact that there is no ideal clock one can compare its performance to. Furthermore, standard statistical tools to assert variations in data sets can not be used, as these require noise distributions independent of the measurement time for the estimator to converge. This is not the case in oscillators, which experience both white noise (independent of time) and flicker noise, the latter varying with the frequency offset and therefore dependent on the measurement time [62].

Allan Deviation The standard statistical tool for assessing oscillator stability is the Allan deviation, $\sigma_y(\tau)$, which is a measure of the frequency stability of the clock in relation to a reference clock. Let $\{y_1, y_2, ..., y_M\}$ be a set of fractional frequency offsets between the observed clock and the reference clock, separated by a period of time τ. The Allan deviation is then given by [62]

$$\sigma_y(\tau) = \sqrt{\frac{1}{2(M-1)} \sum_{i=1}^{M-1} (y_{i+1} - y_i)^2} \tag{4.2}$$

Measuring the Allan deviation over a range of measurement periods τ reveal the time dependency of the clock's stability due to different noise characteristics. Short-term stability may be bad due to white noise, which averages out over longer periods causing better long-term stability. On the other hand, frequency dependent flicker noise typically causes the long-term stability to decrease at some point.

The clocks we will use as time standards for this experiment are commercial off-the-shelf rubidium standard atomic clocks (FS740 GPS Time and Frequency System, see Fig. 4.1), consisting of a $10\,\mathrm{MHz}$ quartz oscillator disciplined on the $6\,834\,682\,612\,\mathrm{Hz}$ hyperfine transition of $^{87}\mathrm{Rb}$.

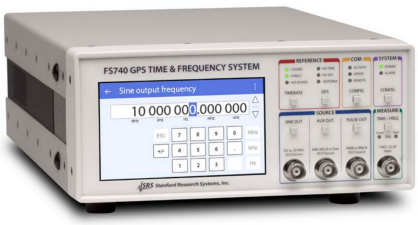

Figure 4.1: Image of the front panel of a FS740 GPS Time and Frequency System, taken from [63].

The listed Allan deviation of these atomic clocks are shown in Fig. 4.2. The claimed fractional frequency deviation of the rubidium timebase is in the order of 1×10^{-11} to

4×10^{-13} over a range of $\tau = 1\,\mathrm{s}$ to $\tau = 10\,000\,\mathrm{s}$. This is interpreted as a root mean square (rms) instability of $\sim 1 \times 10^{-11}$ in frequency samples 1 s apart, which due to noise averaging improves to $\sim 4 \times 10^{-13}$ for frequency samples 10 000 s apart.

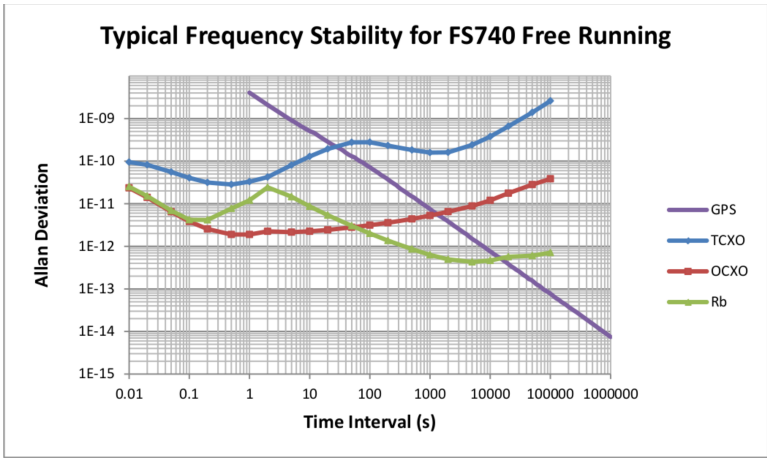

Figure 4.2: The Allan deviation of the FS740 GPS Time and Frequency System, as listed in [63]. The different plots correspond to the possible timebases offered by the system, where the green rubidium line is the only of relevance here. The term *free running* means that the rubidium timebase is not disciplined on the external GPS reference, which is necessary for our measurement.

4.3 Synchronizing Clocks with Entangled Photons

Due to the inevitable frequency instabilities, no two clocks will show the exact same time over longer measurements. This creates the issue of establishing a common time standard between remote locations, which in order to be synchronized requires knowledge on the relative frequency drift of the respective clocks at each location. The synchronization precision of a network of clocks can be improved by conditioning them on a more accurate external time reference. This is for example routinely done with periodic signals from Global Navigation Satellite Systems (GNSS) such as the GPS and GLONASS, consisting of a constellation of satellites carrying highly accurate atomic clocks. Similarly, the remote coincidence detection of photon pairs produced in the SPDC process may be used as a synchronization tool to quantify the amount of which two remote clocks drift relative to each other.

4.3.1 Temporal Correlations in SPDC Pairs

The coincidence detection of signal and idler photons in a SPDC state can be made more precise through the second-order correlation function, which quantify the extent to which

remote photon detection events are temporally correlated. The expression in terms of signal and idler fields is [46, 52]

$$g^{(2)}(\tau) = |\langle 0|\, \hat{\mathbf{E}}_s^-(t)\hat{\mathbf{E}}_i^-(t+\tau)\hat{\mathbf{E}}_s^+(t)\hat{\mathbf{E}}_i^+(t+\tau)\,|\Psi\rangle\,|^2, \tag{4.3}$$

where $\hat{\mathbf{E}}_{s,i}^{(-)}(t)$ and $\hat{\mathbf{E}}_{s,i}^{(+)}(t)$ are the free field operators (see Eq. 2.1), describing photon detection events at respective times t and $t+\tau$. This expression is calculated for a type-2 SPDC source pumped by a cw monochromatic pump laser in [38, 46], yielding the expression

$$g^{(2)}(\tau) \propto |\int d\Omega\, \mathrm{sinc}(\Delta k^z(\Omega)L)\exp(-i\Omega(\tau))|^2. \tag{4.4}$$

The temporal range over which the detection time of two SPDC photons remains correlated is therefore characterized by the joint-spectral amplitude of the SPDC state, which in turn depends on the spectral bandwidth $\Delta\Omega$ allowed by the complex phase-matching conditions. For typical SPDC sources, the width of $g^{(2)}(\tau)$ lies in the sub-ps range [38, 46, 52], meaning that the detection times of the signal and idler photons are temporally correlated withing less than $1\,\mathrm{ps}$.

4.3.2 Timing Resolution of Photon Detection

The photon detection events has to pass through a signal chain typically consisting of the photon detector and a time tagger module, which assigns digital timestamps to the analog signals of the detectors. Both these components add an intrinsic timing uncertainty in the detection event due to electronic jitter. For the photon detector, this jitter is caused by variations in the time it takes to convert the photon detection event into an electronic signal. For the time tagging module, it is similarly caused by variations in the time it takes the electronic pulse from the detector to be converted into digital timestamps. For the use of coincidence detection events in remote clock synchronization, this clearly affects our accuracy in quantifying the temporal drift between the clocks. Fortunately, the variation in these effects follow an approximately Gaussian distribution profile, which means that we can use the statistics of large samples of photon detection events to determine the timing offset with small uncertainty. More precisely, assuming a Gaussian distribution with standard deviation σ and a sample size of N, the standard error in our estimate of the mean value is given by

$$\sigma_{mean} = \frac{\sigma}{\sqrt{N}}. \tag{4.5}$$

As modern SPDC sources have been shown to produce coincidence counts in the order of $10\,\mathrm{Mcps}$ [38], this error can be made almost arbitrarily small.

4.3.3 Identifying the Timing Offset

Once the measurement is running, the two detectors each produce a series of detection events which we can label by their assigned detection times $\{t_i^A\}$ and $\{t_j^B\}$. Formally, we can represent the two time series as functions $a(t)$ and $b(t)$, where

$$a(t) = \sum_i \delta(t - t_i^A) \qquad b(t) = \sum_j \delta(t - t_j^B). \tag{4.6}$$

It is not straightforward to compare the two time series however, as there generally will be a fixed offset ΔT between coincidence events. This offset arise from the different path lengths travelled by the two photons, as well as different start-up times of the time tagging modules. An additional complication is added when the two detection events are recorded with separate clocks, as this introduces a time varying term Δu caused by the relative frequency instabilities in the two clocks. To find the offset between the two time-series, we calculate the cross-correlation function (also called delay histogram)

$$c(\tau) = \sum_t a(t)b(t+\tau),\ \tau = \pm\{0, \delta\tau, 2\delta\tau, ...\}, \tag{4.7}$$

where the discrete time steps, $\delta\tau$, is defined by the time resolution of the data acquisition system. Assuming that the clock drift stays relatively small over the sampling period, we can expect the cross-correlation function to follow a Gaussian distribution due to the timing uncertainty from the electronic jitter. The timing offset is then extracted from the mean of the distribution

$$\Delta T + \Delta u = \frac{\sum_\tau c(\tau)\delta\tau}{\sum_\tau c(\tau)}. \tag{4.8}$$

Assuming then that ΔT remains constant, we can assess the clock drift Δu of remote clocks from the timing offset of the coincidence events over consecutive sampling intervals. The precision in which we can do so primarily depends on the rate of coincidences, the timing resolution $\delta\tau$ and the jitter of the data acquisition system. The coincidence rate and the jitter determines how large the sampling intervals must be to minimize the error in the estimation of the mean. This sampling interval should ideally be small, so that the clock drift over the interval does not impose a significant error in the estimation. Naturally, the timing resolution $\delta\tau$ impose a lower bound on the precision we can obtain.

4.4 Setup and Components

A Type-0 Sagnac Source The entangled photon source we use is a Sagnac source based on a type-0 SPDC process, and is illustrated in Fig. 4.3. It was developed by S. Neumann, U. Galander and D. Ribezzo for a separate project, and conveniently lended to us for this test. The source itself consist of a ppLN crystal ($\Lambda = 19.36\,\mu\mathrm{m}$) which produces wavelength degenerate signal and idler photons with a center wavelength of $1550\,\mathrm{nm}$ at an operating temperature of $\sim 48\,^{\circ}\mathrm{C}$. The crystal is pumped by a cw-laser diode at $\lambda_p = 775\,\mathrm{nm}$, which is focused onto the optimal spot in the crystal by a lens. Inside the Sagnac loop, incident $|V_p\rangle$ states are converted into $|V_s V_i\rangle$ in a type-0 down-conversion process. The overlap of the two pump-directions, where a HWP transforms between $|H\rangle$ and $|V\rangle$ states, result in the maximally entangled Bell state

$$|\Phi^+\rangle = \frac{1}{\sqrt{2}}(|H_i H_s\rangle + e^{i\phi}\,|V_i V_s\rangle), \tag{4.9}$$

where the phase term ϕ can be set accordingly with the HWP in the path of the pump beam. As the pump field and the down-converted modes exit the loop in the same spatial mode, a dichroic mirror is used to reflect the signal and idler modes into a different arm. A filter removes any stray reflections from the pump laser and a second lens collimate the modes before they are coupled into a single-mode (SM) fiber. Here, a dense-wavelength-dual-multiplexer (DWDP) separate states of $\lambda_i = 1545.32\,\mathrm{nm}$ and $\lambda_s = 1554.92\,\mathrm{nm}$ into separate SM fibers. Alignment of the source is performed by maximizing the reflected power of a PBS located in front of a Faraday rotator early in the path of the pump laser. This output port of the PBS will correspond to the back-reflection of the pump laser from the Sagnac loop, and will be maximal when the two directions of the loop overlap perfectly.

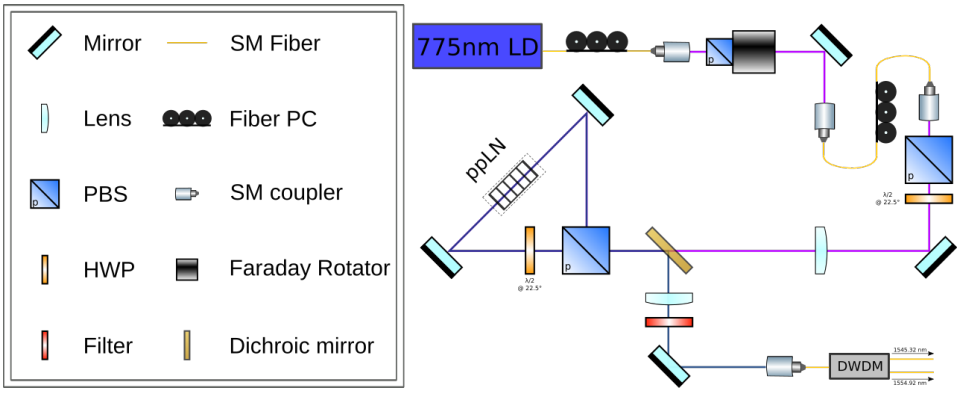

Figure 4.3: Schematic of the type-0 Sagnac source. The setup is further explained in the text.

Polarization Analyzing Modules The two SM fibers leading out of the source can either be coupled straight to the single-photon detectors, or into separate polarization ana-

lyzing modules to verify polarization entanglement. The setup of these modules is depicted in Fig. 4.4, and is practically identical to the setup that was discussed in Section 3.3. The only difference is the addition of a phase-plate in one of the modules, from now on called Alice, which is added as a way to align the polarization bases of the two modules. This is necessary, as stress-induced birefringence in the SM fibers cause unwanted transformations in the polarization of the Bell state. To align the polarization bases, the visibility is first maximized in the H/V basis by a set of polarization controllers mounted on the fibers. These work by twisting the fiber such that the stress-induced birefringence is altered. The phase-plate is itself only a birefringent media with fast axis set to be parallel to the horizontal component of polarization. By tilting the phase plate, keeping the fast axis fixed, the phase between the horizontal and vertical component of the polarization is changed, thus allowing us to maximize the visibility in the D/A basis. Additionally, a motorized HWP was added to the Alice-module for the tests in Section 4.5.2.

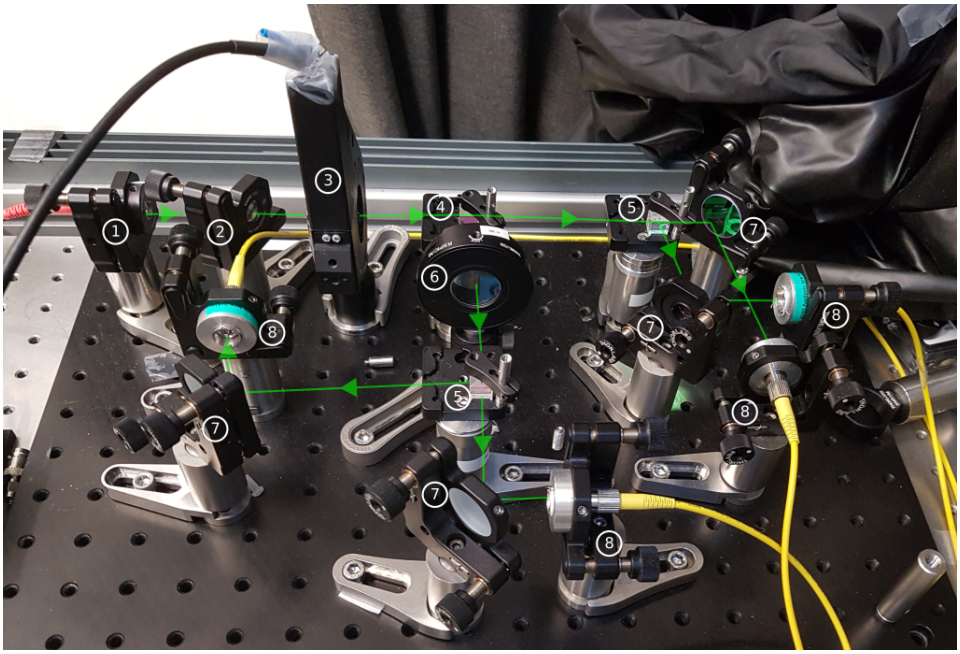

Figure 4.4: Setup for the Alice-module. The Bob-module is identical except for the motorized HWP and the phase-plate. (1) SM collimator, (2) phase-plate, (3) motorized HWP, (4) BS, (5) PBS, (6) HWP, (7) Tip-tilt mirrors for SM fiber coupling, (8) SM fiber couplers. Each single-mode fiber coupler leads to a port on the SNSPD.

Silicon Nanowire Single Photon Detectors Photon detection was performed with two state-of-the-art silicon nanowire single-photon detectors (SNSPDs, Single Quantum Eos). Roughly speaking, the detectors work by operating a thin lattice of superconducting nanowires with a bias voltage just below the critical value for the superconducting phase transition. An incident photon is detected as it is absorbed by the nanowires, locally breaking the superconducting phase causing a quick drop in the voltage. Each SNSPD can be connected

to four separate SM fibers, and are reported with a timing jitter of $\sigma_{det.} \approx 22\,\mathrm{ps}$.

Time Tagger Modules The analog photon detection signals from each respective SNSPD are converted to digital timestamps by two time tagger units (Swabian Instruments ultra 8 series). The internal oscillator of each time tagger unit can be phase locked to the more accurate $10\,\mathrm{MHz}$ pulse from the FS740 time standard. The timestamps assigned by each unit therefore represent the time measured by its local atomic clock. Each time tagger has 8 input ports, and can log $65\,\mathrm{Mevents/s}$ during measurement, which are transferred to a local hard drive via a Gbit-Ethernet connection. The time tagger units are reported with a measured jitter of $\sigma_{t.t.} \approx 11\,\mathrm{ps}$, and a counting resolution of $1\,\mathrm{ps}$.

4.5 Performance Test of the Source and Data Acquisition System

4.5.1 Measuring the Timing Jitter

We first measured the total timing jitter of the setup by locking both time taggers on one atomic clock, thus removing the effect of the relative clock drift. We omitted the polarization analyzing modules and coupled the SM fibers directly into the ports of the SNSPDs to maximize the coincidence counts. The corresponding cross-correlation histogram integrated over a measurement time of $30\,\mathrm{s}$ is presented in Fig. 4.5. The standard deviation of the Gaussian fit implies a combined jitter of the two photon detectors and the two time tagger modules of $\sigma = (37.1 \pm 0.1)\,\mathrm{ps}$. As the total jitter is essentially the convolution of the Gaussian distribution from each individual component, we may give an estimate for the jitter of the individual components from

$$\sigma = \sqrt{2\sigma_{t.t.}^2 + 2\sigma_{det.}^2}. \tag{4.10}$$

If we assume $\sigma_{det.} = 2\sigma_{t.t}$, which is reasonable from the claimed jitter of the components, we get

$$\sigma_{t.t} = \frac{\sigma_{det.}}{2} = \frac{\sigma}{\sqrt{6}} = 15\,\mathrm{ps}. \tag{4.11}$$

This is in reasonable agreement with the values listed in Section 4.4.

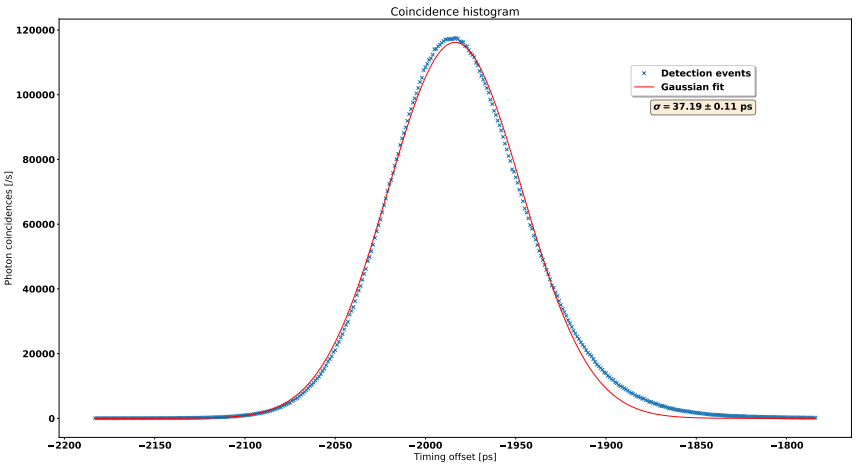

Figure 4.5: Histogram over the time offset of photon detection events, recorded with time taggers conditioned on the same atomic clock. The plot shows photon counts integrated over 30 s. A Gaussian fit suggests a total jitter of (37.1 ± 0.1) ps.

4.5.2 Test of Polarization Entanglement

To verify the polarization entanglement produced by the source, we performed a test of the visibilities in each basis of the detector module. This was done by inserting a motorized HWP in front of the Alice-module (see Fig. 4.4), which can be rotated in order to show the dependency of the visibilities on the detector bases. Given that we successfully mapped the Bell state from the source to the detection modules, the effect of the HWP transformation on the probability of a coincidence count between each detector in the H/V basis is

$$\begin{aligned} P_{\Phi^+}(H_A H_B) &= |\langle\Phi^+| HWP(\Theta)_A |H_A H_B\rangle|^2 = \cos^2 2\Theta \\ P_{\Phi^+}(V_A H_B) &= |\langle\Phi^+| HWP(\Theta)_A |V_A H_B\rangle|^2 = \sin^2 2\Theta \\ P_{\Phi^+}(H_A V_B) &= |\langle\Phi^+| HWP(\Theta)_A |H_A V_B\rangle|^2 = \sin^2 2\Theta \\ P_{\Phi^+}(V_A V_B) &= |\langle\Phi^+| HWP(\Theta)_A |V_A V_B\rangle|^2 = \cos^2 2\Theta \end{aligned} \tag{4.12}$$

As the $|\Phi^+\rangle$ state remains perfectly correlated in the D/A basis, i.e.

$$HWP(22.5°)_A HWP(22.5°)_B |\Phi^+\rangle = \frac{1}{\sqrt{2}}(|D_A D_B\rangle + |A_A A_B\rangle), \tag{4.13}$$

where the HWP transformations here should be identified with the passive HWPs in the D/A arm of the Alice- and Bob-modules, a calculation of the coincidence probabilities returns the same expressions as for the H/V basis. This is verified in Fig. 4.6, showing the

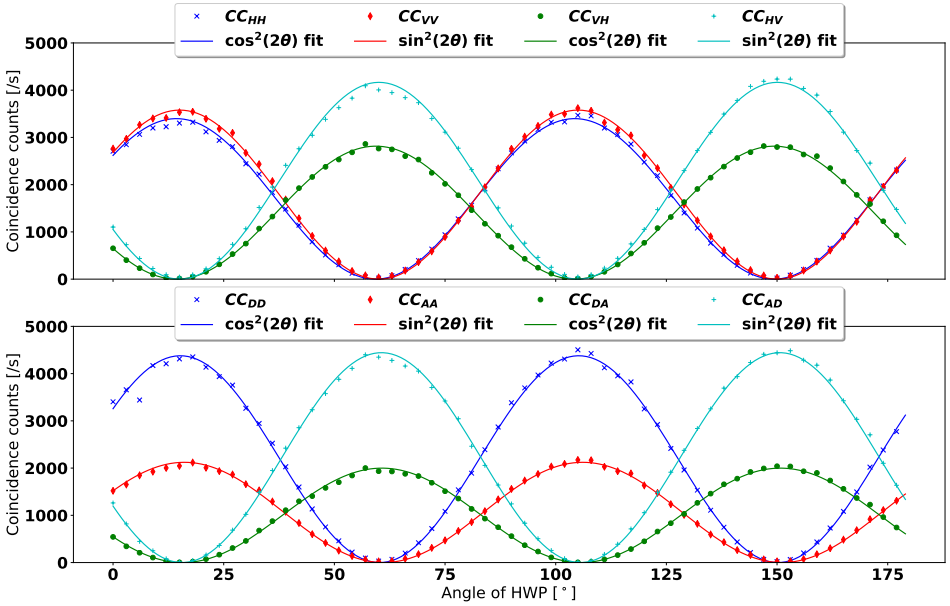

Figure 4.6: Coincidence rates between detectors in the H/V and D/A basis. Each data point correspond to a 3° increment in the rotation of a HWP, and was averaged over a $10\,\mathrm{s}$ integration time. The interpolation lines follow from a least squares fit.

angular dependence of the coincidence rates as the HWP is rotated in increments of 3°, where each data point correspond to the average coincidence rate over a $10\,\mathrm{s}$ integration time. The offset of the $\cos^2$ and $\sin^2$ fits simply indicate that the initial position of the HWP was not aligned with the horizontal axis. We can pinpoint the offset somewhere close to $\Theta_0 \approx 15^\circ$. The different amplitudes of the coincidence rates is likely caused by different coupling efficiencies into the SM fibers, and is not of particular importance. The visibility of the H/V and D/A basis follow straight from using Eq. 2.24, yielding a maximal visibility of $V_{\mathrm{H/V}} = 98\%$ and $V_{\mathrm{D/A}} = 99\%$, which is more than enough to demonstrate entanglement.

During the same measurement we can investigate the explicit dependency of different basis choices on the violation of Bell's inequality. Let C_{ij} denote the coincidence rate between detectors i, j as the HWP is rotated by an angle Θ, where $i \in \{H, V, D, A\}$ denotes the detector arms in the Alice-module and identically for j the detector arms in the Bob-module. The polarization angles in the Bob-module are fixed at $0^\circ, 90^\circ, 45^\circ$ and -45° corresponding to the H, V, D and A detector arms respectively, while the measurement in the H, V, D and A arm of the Alice-module corresponds to polarization angles $2\Theta, 90^\circ + 2\Theta, 45^\circ + 2\Theta$ and $-45^\circ + 2\Theta$ as the HWP is rotated. The four basis measurements necessary for the CHSH inequality (Eq. 2.22) can therefore be realized through the combinations

$$E(2\Theta, 0^\circ) = (C_{HH} + C_{VV} - C_{HV} - C_{VH})/N(2\Theta, 0^\circ)$$
$$E(2\Theta, 45^\circ) = (C_{HD} + C_{VA} - C_{VD} - C_{HA})/N(2\Theta, 45^\circ)$$
$$E(45^\circ + 2\Theta, 0^\circ) = (C_{DH} + C_{AV} - C_{DV} - C_{AH})/N(45^\circ + 2\Theta, 0^\circ)$$
$$E(45^\circ + 2\Theta, 45^\circ) = (C_{DD} + C_{AA} - C_{DA} - C_{AD})/N(45^\circ + 2\Theta, 45^\circ)$$

where $N(\alpha, \beta)$ is simply the sum of the corresponding coincidence rates.

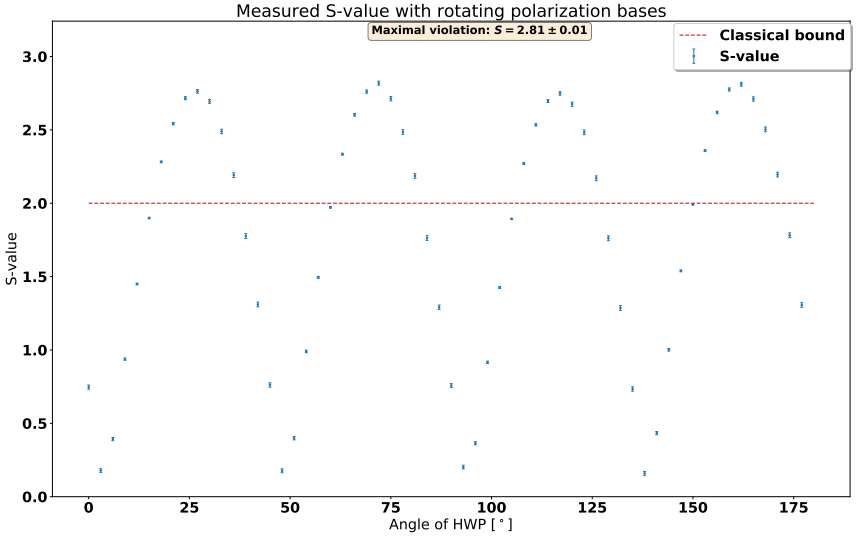

Figure 4.7: Rotating the HWP shows the explicit dependency of the measurement bases on the violation of Bell's inequality. Each data point correspond to a 3° increment in the rotation of a HWP, and was averaged over a 10 s integration time.

The maximal violation should then be obtained for $\Theta = 11.25^\circ + \Theta_0 \approx 25.25^\circ$, corresponding to the linear polarization angles $\alpha = 0^\circ, \beta = 22.5^\circ, \alpha' = 45^\circ$ and $\beta' = 67.5^\circ$. This is confirmed in Fig. 4.7, where the S-value in Eq. 2.22 is plotted using the same measurement data as in Fig. 4.6. The periodicity of the S-value follow naturally from the symmetry of $|E(\alpha, \beta)| = |E(\alpha + \pi/2, \beta)|$. The maximal violation is found to be $S = 2.81 \pm 0.01$, where the error bars correspond to a 1σ uncertainty. This is calculated from the Gaussian error propagation of the coincidence rates, assuming a Poissonian distribution so that $\Delta C_{ij} = \sqrt{C_{ij}}$. The complete expression is then given by [64]

$$\Delta S = \sqrt{\Delta E^2(\alpha, \beta) + \Delta E^2(\alpha', \beta) + \Delta E^2(\alpha, \beta') + \Delta E^2(\alpha', \beta')}, \tag{4.14}$$

where

$$\Delta E(\alpha, \beta) = \sqrt{\frac{1}{N(\alpha, \beta)}(1 + E(\alpha, \beta)^2)}. \tag{4.15}$$

4.6 Test of Clock Synchronization with SPDC

Having verified the performance of the individual parts of the experimental setup, we set out to test the clock synchronization scheme. An overview of the setup we use is illustrated in Fig. 4.8. For these tests, we again coupled the SPDC modes from our entangled photon source directly to the SNSPDs. The respective time tagger units were now phase locked on separate atomic clocks, so that the time offset of the coincidence peak drifted with the frequency shift of the two clocks. Additionally, a 1 Hz signal from a function generator was split up to each time tagger. This serves as a second estimation of the clock drift, which we can use for comparison with the coincidence peak.

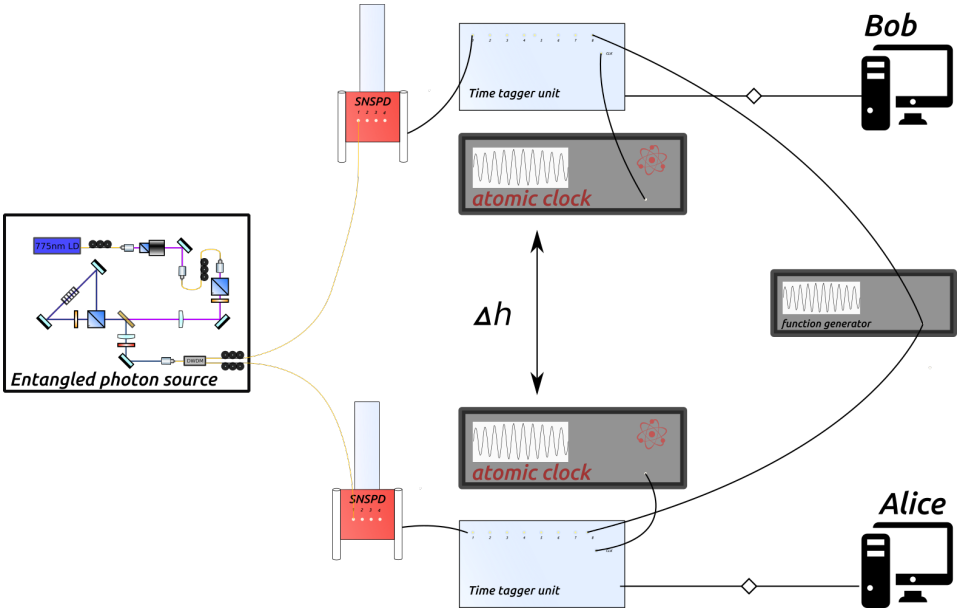

Figure 4.8: Schematic of the setup for the clock synchronization test. See the text for further explanation.

By using 37.1 ps as the standard deviation of the timing accuracy of each coincidence event, a theoretical synchronization precision greater than 1 ps demands (from Eq. 4.5)

$$N \geq \frac{(37.1\,\mathrm{ps})^2}{(1\,\mathrm{ps})^2} = 1376.4.$$

A conservative estimate of the average coincidence counts produced by our setup is $\sim$ 100 000 cps (see e.g. Fig. 4.5), thus demonstrating that this bound is easily reached.

We measured the relative clock drift of two freely drifting atomic clocks over three con-

secutive intervals. During the first and third measurement we stationed both clocks at the same elevation, while for the second measurement one clock was lifted to an elevation of $4\,\mathrm{m}$. We call this clock B, and denote the fractional frequency shift between the two clocks as $\delta f/f_A = (f_B - f_A)/f_A$. We expect a fractional frequency shift caused by gravitational time dilation over this height difference of $\delta f/f_A = 4.4 \times 10^{-16}$. The relative clock drift over the measurement intervals was estimated by integrating coincidence counts over $1\,\mathrm{s}$. For each sample, this gives a value for the timing offset $\Delta T_i + \Delta u_i$. By subtracting consecutive offsets we then get an estimate of the relative clock drift over each sampling period, assuming that ΔT_i remains constant. Dividing this temporal drift by the $1\,\mathrm{s}$ sampling time gives the fractional frequency deviation of the two clocks.

With this sampling time, the fundamental time resolution of the synchronization scheme is given by the $1\,\mathrm{ps}$ counting resolution of the time taggers. To detect a shift in the clock drift caused by gravity, we must therefore measure for a minimum of $1\,\mathrm{ps}/4.4 \times 10^{-16} = 2273\,\mathrm{s}$. The fractional frequency deviations over $10\,000\,\mathrm{s}$ intervals are shown for the three measurements in Fig. 4.9. Here, the statistical uncertainties from the standard deviation of the mean are too small to be visible in the plot. The average fractional frequency deviation over the entirety of the three individual measurements, corresponding to the dashed lines in Fig. 4.9, are listed in Table 4.1. The observed frequency shifts between each measurement is in the order of 10^{-12}, which is clearly not the precision we need to measure time dilation. Rather, this value corresponds well to the rms frequency instabilities of the clocks, as predicted by the Allan deviation (see Fig. 4.2).

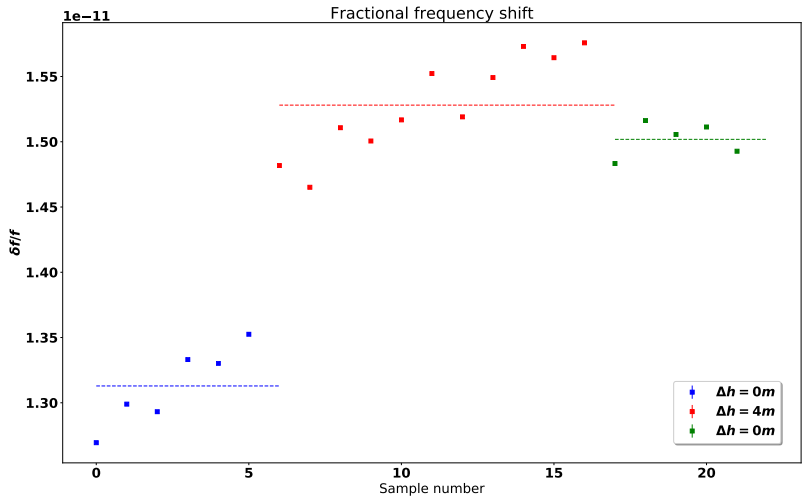

Figure 4.9: Measured frequency shifts with the coincidence detection of entangled photons of the two atomic clocks at different heights. Each point corresponds to $10\,000\,\mathrm{s}$ of measurement data. The statistical uncertainties are in the order of 1×10^{-15} and therefore too small to be visible on the plot.

Table 4.1: Average fractional frequency shifts over the three consecutive measurements, with statistical uncertainties.

Meas. #	Total sampling time	Δh	$\delta f / f_A$
1	60 000 s	0 m	$(13.127\,61 \pm 0.000\,51) \times 10^{-12}$
2	110 000 s	4 m	$(15.321\,79 \pm 0.000\,46) \times 10^{-12}$
3	50 000 s	0 m	$(15.063\,41 \pm 0.000\,19) \times 10^{-12}$

In Fig. 4.10, the clock drift obtained by each 1 s sampling time during measurement 1 was used to calculate a corresponding Allan deviation of the two clocks. This is compared with the clock drift measured by a 1 Hz signal from the function generator. The latter was obtained by using the coincidence events as an initial synchronization reference, and then simply comparing the time offset of subsequent pulses recorded by each time tagger. Over averaging times slightly larger than 10 s, these independent measurement tools show good correspondence, supporting the validity of using SPDC for clock synchronization.

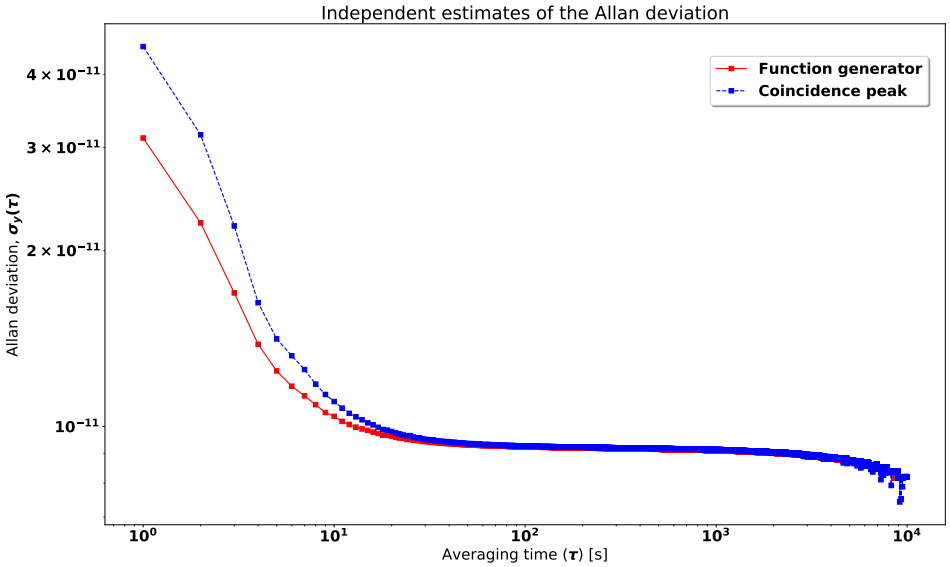

Figure 4.10: Comparison of the Allan deviation obtained by using the two-photon coincidence peak and the 1 Hz signal from a function generator as estimates for the frequency instability of the two clocks.

It was discovered in the aftermath of these measurements that the temperature control in the room contributes to a significant change in the optical path lengths of the SM fibers. This can be seen in Fig. 4.11, where the coincidence peak was measured with the two time taggers locked to the same timing standard. At this point no clock drift is present, and the drift of the coincidence peak must therefore be attributed to ΔT_i, caused by variations in the optical path length. The periodic trend that is observable in the slow negative drift and the subsequent sharp rise, correlate well with the duty cycle of the temperature

controller in the room, which was measured to $\sim 50\,\mathrm{min} = 3000\,\mathrm{s}$ in [43]. This likely explains the initial offset in the Allan deviation of the two methods, as the coaxial cables from the function generator are much better isolated than the SM fibers, and therefore not as sensitive to temperature fluctuations. Whether or not this had a significant effect on the former measurements is hard to say, but likely these fluctuations average out for the $10\,000\,\mathrm{s}$ samples, which the Allan deviation also indicates. Although we were aware of this potential issue in the beginning of the experiment, the size of the effect was surprising. Certainly, it serves as a reminder to the small orders of magnitude we are operating at.

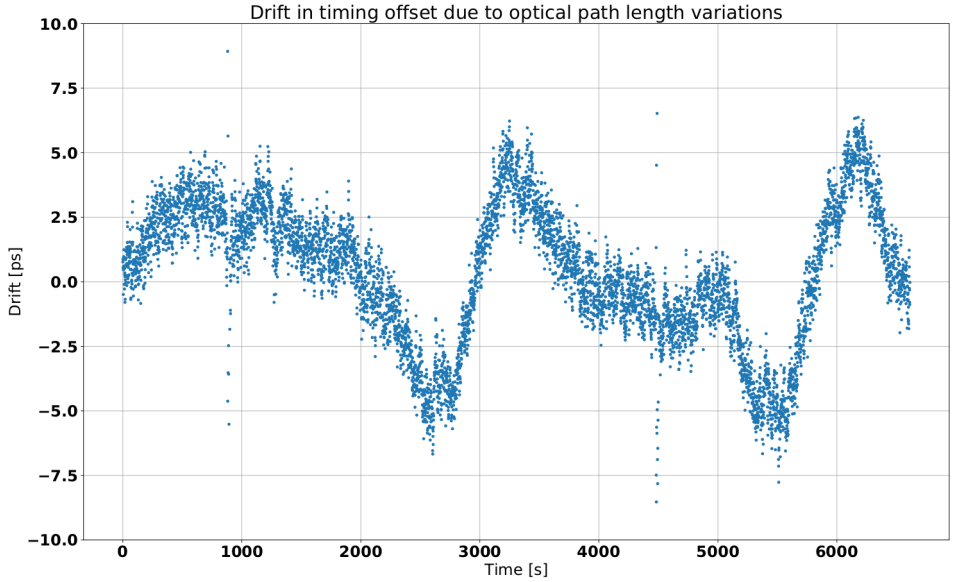

Figure 4.11: Phase locking both time taggers to the same atomic clock shows the drift in the coincidence peak due to variations in the optical path length, likely due to the temperature controller in the laboratory.

Finally, it is natural to compare the Allan deviation we measure with the listed Allan deviation of the atomic clocks, which was shown in Fig. 4.2. For the sampling periods ranging from $1\,\mathrm{s}$ to $10\,000\,\mathrm{s}$, the rms frequency instability is roughly one order of magnitude larger for our measurements. This is not necessarily a symptom of the measurement tool however, as the Allan deviation will depend largely on the timing standard that is used as reference. We don't have this information for the given graphs, but in general it is recommended to use a reference standard for these measurements an order of magnitude more accurate than the device that is being tested [62]. It is thus not implausible that this explains the slightly worse Allan deviation we obtain by using the same timing standard as both reference and sample.

4.7 Discussion

It is clear from the results of the former section that the initial prospect of verifying time dilation over the small height differences available in the lab was quite misguided. For more experienced researchers within time and frequency metrology, this would also likely be obvious from the outset, as the Allan deviation of the two clocks predict rms frequency instabilities of the order of 10^{-12} over $\tau = 10\,000\,\mathrm{s}$, orders of magnitude greater than the frequency shift caused by gravity. Our hope was that these instabilities followed some Gaussian distribution and therefore could be averaged out over longer measurements, but the noise profile of atomic clocks is clearly more complex than we were aware of. In the end, the synchronization scheme can at best only reproduce the actual drift of the two clocks, and does not offer anything in terms of a better frequency stability. Nevertheless, the Allan deviation we obtain with the synchronization scheme is a good indicator that we accurately can measure the real drift of the two clocks. To measure time dilation effects, this leaves us with the option to either use better timing standards or move the experiment to larger potential differences in the gravitational field. The latter may be accessible in the not so distant future, as numerous groups have been working towards launching small scale QKD satellites for low earth orbits (LEO). At these scales, time dilation effects are perhaps significant enough to be measured with this synchronization scheme. A straight forward calculation of the expected frequency shift is out of scope for this thesis however, as the expressions quickly get more complicated outside of the weak-field approximation. Additionally, for a LEO satellite the time dilation effects of special relativity must be included, which for some cases dominates gravitational effects. These calculations are discussed in greater detail in [65], but I could not find any direct estimates for LEO satellites.

We can make some rough qualitative considerations on the obtainable synchronization precision over a ground-to-satellite link however, notwithstanding the additional technical difficulties such a setup would entail. Several feasibility studies have been published on the topic of satellite QKD missions [e.g. 56–58]. Basing here the argument on parameters listed in [57], it is reasonable to assume a total timing jitter of the detector and time tagger system of $40\,\mathrm{ps}$, similar to the setup demonstrated in this chapter. Count rates from entangled photon sources are readily realized in the order of $10\,\mathrm{Mcps}$, and with a total link attenuation of $60\,\mathrm{dB}$ for a LEO satellite, this corresponds to a coincidence rate of $\sim 10\,\mathrm{cps}$. Over $1\,\mathrm{s}$ sampling times, this gives a theoretical synchronization precision of $12.6\,\mathrm{ps}$. In a historical perspective however, the trend is a yearly doubling of the source pair rate [38], so this factor may be improved drastically in the years to come. In this scenario, an additional difficulty arise from the path length variations due to atmospheric turbulence and the orbit of the satellite. Atmospheric turbulence alone is expected to add a jitter in the order of $\sim 10\,\mathrm{ps}$, while it is not straightforward to predict how well the path length variations of the orbit can be compensated for. Furthermore, a typical link connection time of $\sim 220\,\mathrm{s}$ per orbit places some limiting restrictions on the amount of statistics that can be collected.

Finally, it is reasonable to ask if this scheme actually offer something new in terms of time

and frequency metrology. To discuss this, I do not possess enough insight into the field of metrology, but some thoughts from the point of view of quantum entanglement experiments and QKD are in order. First of all, the predictions of quantum mechanics in different gravitational potentials is one of the areas of fundamental physics that remain largely unexplored, yet are within our technological capabilities. A natural benefit of testing time dilation with such synchronization schemes is that it can be used to test the interplay of entanglement and gravity. As some theories predicts gravitational decoherence in entangled photon pairs measurable over these scales [66], the topic is certainly worth investigating. Furthermore, in terms of QKD, this synchronization protocol has already proved useful to obtain greater synchronization accuracies than with time taggers disciplined on pulse-per-second GPS signals. For QKD schemes based on time-bins, this synchronization precision is critical, and the scheme will therefore likely be used for the free-space link I describe in Chapter 5. For the remainder of this thesis however, I will not be addressing it any further.

Chapter 5

Establishing a High-Dimensional Free-Space QKD Link

The free-space implementation of QKD links is absolutely necessary for the technology to reach a state where users can communicate securely over a global scale. A central limitation to the implementation of polarization based QKD over free-space links is the low signal-to-noise ratio introduced by the bright background under daylight conditions. Previous demonstrations of daylight QKD has overcome this barrier by various combinations of temporal, spatial and spectral filtering techniques, for example by using narrow bandpass filters, small field of view and pulsed detection windows [67–69]. Still, secure key rates remain orders of magnitudes lower than under optimal conditions at night. An alternate technique was introduced by our research group at IQOQI [70], where it was demonstrated that going to a higher-dimensional entangled state space can be exploited to increase the signal-to-noise ratio under noisy background conditions. This experiment can be considered as the natural continuation, where we test the feasibility of using the post-selection free Franson interferometer for a daylight QKD protocol over $10.2\,\mathrm{km}$ in free-space across the skyline of Vienna. In this chapter, I present considerations and design choices for the free-space implementation of this setup, along with some preliminary measurements demonstrating Franson interference in the lab and testing the transmission stability of our tracking scheme.

5.1 Improved Noise Resilience from a Higher-Dimensional State Space

Before I discuss our experimental setup, I briefly explain the findings of [70], which provides the fundamental motivation for this experiment. First of all, limiting noise is a key factor in robust protocols for distributing entanglement. Verifying the distribution of a polarization entangled state requires for instance an average visibility higher than 50% in two bases. Noise in the form of dark counts and background photons cause *accidental coincidences* between all detectors and therefore lower the visibility of the state, possibly destroying entanglement in the sense that it is impossible to verify its existence. As noise is a very real complication present in the transition from ideal laboratory conditions to the real world, developing noise robust protocols is desirable for reaching the full potential of QKD.

To verify the existence of entanglement in higher-dimensional systems, it is convenient to reconstruct the density matrix of the system from the experimental data. These matrix elements can be reconstructed from the normalized coincidence rate $\rho_{ij} = CC_{ij}/CC_{tot}$. For a maximally entangled polarization state $|\Phi^+\rangle$, a measurement would ideally return only non-zero diagonal elements, corresponding CC_{HH} and CC_{VV} coincidences. However, accidental coincidences will inevitably occur due to noise, contributing to non-zero off-diagonal elements and lowering the overall visibility of the state. This is typically modeled through the white-noise model,

$$\hat{\rho} = p\,|\psi\rangle\,\langle\psi| + \frac{1-p}{d^2}\mathbb{1}_{d^2}, \tag{5.1}$$

where p classifies the amount of noise (zero for $p = 1$) and d is the dimensionality of the state. The key insight is now that accidental coincidences spread evenly over all d^2 elements of the density matrix, while *true coincidences* corresponding to entangled photons will divide only across the d diagonal elements. As the amount of accidental coincidences in principle is independent of the dimensionality of the state, going to higher-dimensional entangled states can therefore help to reveal entanglement in noisy scenarios. In [70], this principle was experimentally verified in the laboratory frame, using the post-selection free Franson interferometer to project energy-time entanglement onto maximally correlated time-bin states. The higher-dimensional characteristics of this system is realized by *fine-graining* the time-bin states, which essentially boils down to discretizing a time-frame into d time-bins. Varying d then corresponds to adjusting the dimensionality of the state. By simulating noisy background conditions with adjustable LEDs, it was shown that increasing the fine-graining of the time-bin states reveal entanglement where coarser time-bins could not. However, as this only allows the detection of one pair of photons per time-frame, it introduces a trade-off in terms of the optimal dimension and time-frame for the secure key rate. Smaller time-frames allow higher coincidence rates but also fewer dimensions. This is a relationship that in turn need to optimized for the given noise conditions,

and will for example be different for operation during night and day.

5.2 Proof-of-Principle: Franson Interference in the Lab

As the free-space implementation of the receiving interferometer at the time of writing this thesis is not fully ready, I here show a proof-of-principle measurement of Franson interference with both interferometers located in the lab. The principles described in this section are directly transferable to the free-space scenario, only adding the extra difficulty in dealing with the effects of the turbulent atmosphere on the beam.

5.2.1 A Type-2 Sagnac Source

The source designed for this experiment is illustrated in Fig. 5.1, and was developed by L. Bulla and O. Kohout for this experiment. It is a Sagnac source consisting of a $2\,\mathrm{cm}$ long ppKTP crystal, which produces non-degenerate signal and idler photons at a center wavelength of $810\,\mathrm{nm}$. A thermo-electric heater (TEH) keeps the crystal at the necessary operating temperature of $\sim 32^{\circ}\mathrm{C}$. The crystal is pumped by a continuous wave laser diode at $\lambda_p = 404.5\,\mathrm{nm}$, which is focused by a lens onto the optimal spot in the crystal. Inside the Sagnac loop, incident $|H_p\rangle$ states are converted into $|V_s H_i\rangle$ in a type-2 SPDC process. The overlap of the two pump-directions, where a HWP transforms between $|H\rangle$ and $|V\rangle$ states, result in the maximally entangled Bell state

$$|\Psi^+\rangle = \frac{1}{\sqrt{2}}(|H_i V_s\rangle + e^{i\phi}\,|V_i H_s\rangle), \tag{5.2}$$

where the phase ϕ can be set by rotating a combination of HWPs and QWPs placed in the path of the pump laser. Alignment of the source is done by looking at the spatial overlap of the incident pump laser with the back-reflected mode (see Fig. 5.1). This step is explained more detailed in [43].

The signal and idler modes exit in separate ports of the PBS, and a dichroic mirror is used to separate the idler from the pump beam. Two lenses are placed in the path of the signal and idler modes for collimation, as well as additional filters to remove any unwanted residual reflections from the pump. These are then coupled into SM fibers, transmitting the modes to the two interferometers. Each SM fiber is mounted with a set of polarization controllers, which are used to manipulate the stress-induced birefringence in the fiber. We use this as a polarization transformation to obtain the necessary $|\Phi^{\pm}\rangle$ state for the post-selection free Franson interferometer.

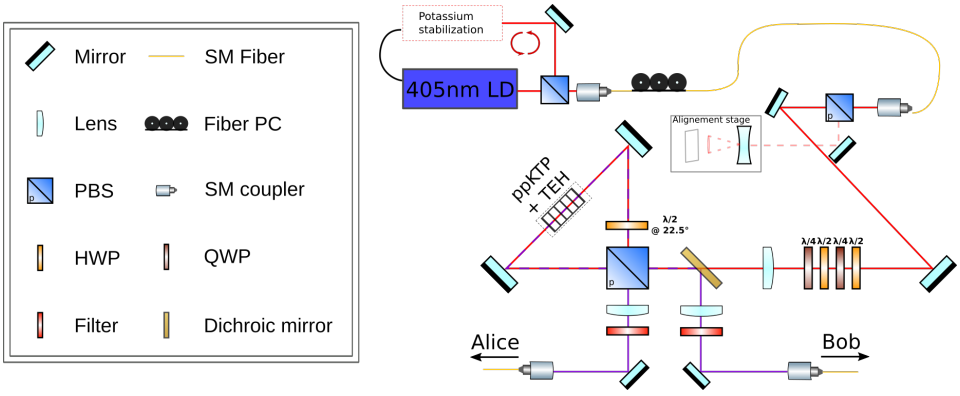

Figure 5.1: Schematics of the type-2 Sagnac source. The setup is explained further in the text.

5.2.2 Implementation of a Post-Selection Free Franson Interferometer

Our entanglement analyzing modules consist of two post-selection free Franson interferometers. In the following, I will refer to the two interferometer modules as Alice and Bob, where Bob is the interferometer that will be used for the receiver station in the free-space experiment. In the lab experiment, these modules are fairly similar, while the Bob interferometer will need further modifications for the free-space setup. Additionally, I will refer to the signal and idler modes as the quantum signal.

A schematic of the Bob-interferometer is illustrated in Fig. 5.2. It is in principle identical to the post-selection free Franson interferometer discussed in Section 3.4.1, with certain additional features. Mainly, this is the addition of a 775 nm stabilization laser (Toptica DLC DL pro), the placement of two 4f lens systems in the long arm of the interferometer and the alignment stage, which is only used to prepare for measurements. The 4f systems is added as a step to improve the angle of arrival stability of the interferometer, which will be a central issue in the free-space implementation (see e.g. [71]). By placing the PBSs and mirrors in the focus of the two 4f systems, the 4f system ensures that the short and long beam paths overlap even if the beam arrives at an angle. This calculation is shown in Appendix A.

5.2.3 Stabilizing the Interferometer Path Length

To consistently obtain Franson interference, the phase shift obtained from the longer path must be kept stable. However, even minor changes in the temperature gradients within the laboratory cause thermal expansion in the optical components enough to significantly decrease the interference visibility, thus demonstrating the need for active path length

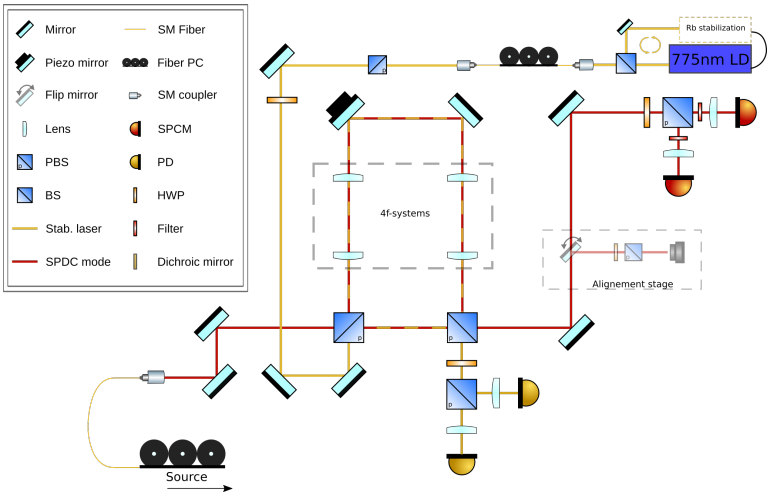

Figure 5.2: Schematic of our implementation of the post-selection free Franson interferometer. The additional features of a stabilization laser and two 4f systems is explained in the text.

stabilization.

The stabilization scheme we employ consist of a feed-back loop between the interference signal of a secondary laser traversing the interferometer, and a piezo mirror which by applying different voltages continuously adjust the optical path length. For the Bob interferometer, we use a $775\,\mathrm{nm}$ laser diode, while for the Alice interferometer, the pump laser itself is used. The stabilization laser is prepared in a $|D\rangle$ state by a sequence of a PBS and a HWP, such that it splits evenly between the two interferometer arms. As this laser enters the interferometer from a different port on the first PBS than the quantum signal (see Fig 5.2), the vertical polarization traverses the short path and the horizontal polarization the long path. Consequently, it also recombines at a different output than the quantum signal. However, as there is always a slight inefficiency in the reflection arm of a PBS, narrow bandpass filters are added to the single-photon detectors, ensuring that any $775\,\mathrm{nm}$ signal from the stabilization laser is removed.

Using the same principle as with the quantum signal, we obtain interference by measuring the output state of the stabilization laser in the D/A basis, employing the usual combination of a HWP rotated by $22.5°$ and a PBS. A photo diode (PD) is placed in each arm of the final PBS, converting the interference signal to a current. This current is in turn fed into a PID-controller, feeding its response through a set of high-voltage amplifiers and into the piezo mirror, completing the feed-back loop. The parameters of the PID-controller are then adjusted to keep the interference signal stable, and thus also the optical path length. As we use a shorter wavelength for the stabilization laser, we ensure that the phase is stable also for the quantum signal.

A key requirement for the scheme to work as intended is that the wavelength of the sta-

bilization laser itself is kept stable. Similar to the principal concepts of atomic clocks, we use hyperfine transition lines as frequency standards for our stabilization lasers. A more detailed description of this setup is however beyond the scope of this thesis. For the $775\,\mathrm{nm}$, we use a compact saturation spectroscopy module with a Rb frequency reference (CoSy, TEM Messtechnik). For the Alice interferometer, we use the pump laser itself as stabilization laser by splitting it up with a 50-50 beam splitter. The wavelength stabilization for this is ensured by a potassium based absorption cell built by O. Kohout. For both implementations, a PID-controller adjusting the input current to the lasers ensures that the wavelength stays on the hyperfine transition.

5.2.4 Data Acquisition

Two single-photon counting modules (SPCM-800-11, Excelitas Technology) are used for the detection module in each interferometer. These have a sensitive area of $180\,\mu\mathrm{m}^2$ and timing jitter in the order of $\sim 350\,\mathrm{ps}$. A local time tagger module at each interferometer (TTM8000, Austrian Institute of Technology) assign a timetag to the rising edge of the electronic SPCM signal. These can each support up to eight external inputs with a timing resolution of $82.3\,\mathrm{ps}$, which defines the smallest time-bin we can use for fine-graining. The time taggers are able to process $25\,\mathrm{Mevents/s}$, which are transferred to hard-drives via a Gbit-ethernet connection. For the laboratory measurement, the time taggers could be disciplined to each other, removing the need for any clock synchronization protocol.

5.2.5 Experimental Routines

First Steps: Aligning the Interferometer Aligning an interferometer from scratch require a certain methodology, and above all patience. The first coarse alignment is done by shining a strong coherent laser through the interferometer. We place all optical elements, with the exception of the two 4f systems, so that the beam is coarsely led through the desired path. All elements are placed on similar pedestals, such that the center height is $7\,\mathrm{cm}$ throughout the interferometer. The mirrors and beam splitters can additionally be tip-tilted through two axes to adjust the vertical and horizontal angle of reflection. Then, by using two irises as crosshairs, we adjust the tilt of all elements such that the height of the laser stays centered throughout the setup. The long path of the unbalanced Mach-Zehnder interferometer must now be adjusted so that the two paths completely overlap when rejoined. This is done by observing the beam profile with a CCD camera (SP620U Spiricon, Ophir Optics), placed at the end of the alignment stage (see Fig.5.2), which is entered by the deflection of a flip mirror. Here, as in the detectors arms for the quantum signal, a HWP oriented at 22.5° and a PBS projects the polarizations onto the D/A basis. When the interferometer is misaligned, the different angles of the two beams cause spatial interference fringes on the camera (see Fig. 5.3). The mirrors in the long arm are therefore tilted until the interference fringes disappear. The quality of the alignment can now be quantified by applying a sinusoidal voltage to the piezo mirror, leading to periodically constructive and

destructive interference patterns at the camera. Measuring the contrast between the maximum and minimum beam power at the position of the camera, we can assert a visibility to the overlap, which preferably should be above 90%. When this is obtained, we insert the first 4f system and adjust the position and tilt of the two lenses until the interference visibility is back, before we repeat the procedure with the second 4f system. After this procedure, the interferometer stays roughly aligned over time, and it is enough to adjust the tip-tilt mirrors of the long path only slightly to reobtain the alignment.

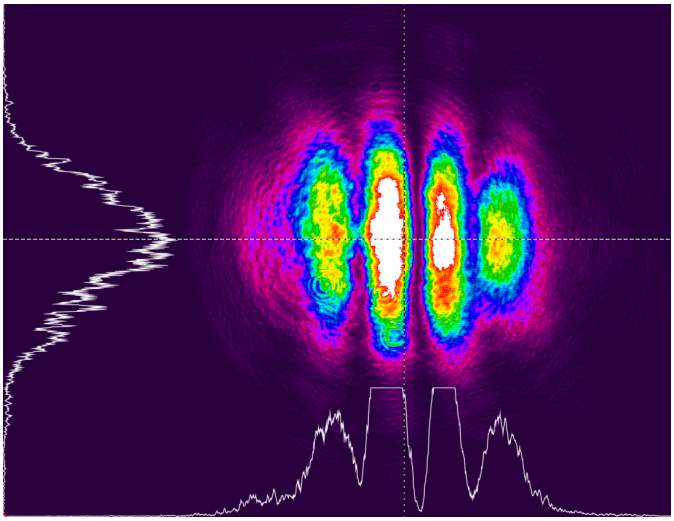

Figure 5.3: The overlap of the long and the short interferometer arms is observed with a *Spiricon* CCD camera. A screenshot of the supporting *BeamGage*-software shows spatial interference fringes in the beam power, characteristic of two misaligned beams.

When the interferometer is aligned, it remains to align the coupling onto the single-photon detectors. First, we attenuate the laser with multiple absorptive filters, so that we don't saturate the SPCMs. The beam then needs to be focused onto the sensitive area of the detector surfaces. This is largely an iterative procedure, where we observe the detector signal while adjusting the tip-tilt mirror in front of the module and translate the lenses until the focus is optimized.

Establishing Common Polarization Bases The last preparatory step is to ensure that the $|\Psi^-\rangle$ state is mapped correctly to a $|\Phi^-\rangle$ state after the SM fibers. This step is nicely visualized and described in [43], and we use here essentially the same method. The trick we use relies on the fact that the two modes share a common phase which can be tuned by the pump phase. If we insert two polarizers oriented at 45° after the SM fibers, the coincidence counts of the $|\Phi^-\rangle$ state should be at a minimum, i.e.

$$P_{\Phi^-}(DD) = |\langle D_i D_s|\Phi^-\rangle|^2 = 0. \tag{5.3}$$

Tuning the pump phase correspondingly, we obtain the desired mapping.

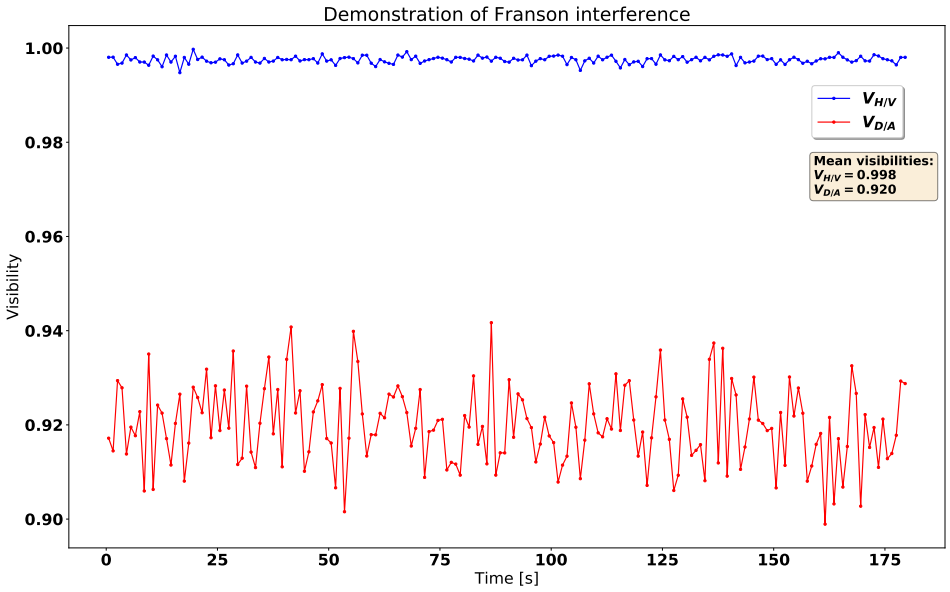

Figure 5.4: Visibilites in the H/V and D/A basis over two consecutive $3\,\mathrm{min}$ intervals. Each point corresponds to the visibility averaged over $1\,\mathrm{s}$.

5.2.6 Demonstration of Franson Interference

Fig. 5.4 shows the result from two consecutive $3\,\mathrm{min}$ measurements of the visibility in the H/V and D/A basis. The H/V visibility is obtained by rotating the HWPs in front of the two detector modules into the $0°$ position. At this position, the polarization can be used to label the path taken through the interferometer, and the measured coincidences therefore simply corresponds to a normal polarization visibility. The D/A visibility corresponds to the Franson interference we obtain by setting the HWPs to the $22.5°$ position. The two visibilities are respectively averaged to $V_{H/V} = 99.8\%$ and $V_{DA} = 92.0\%$. The larger oscillations in the D/A basis is likely due to minor phase shifts caused by thermal fluctuations and the following corrections by the piezo mirror. This does not affect the H/V visibility, which is not dependent on the phase shift obtained over the two arms.

5.3 Free-Space Considerations

Having showed that our setup works in the lab, the next step is to implement the setup for use in a free-space link. In the following sections I discuss some of the challenges this entails, and the following design choices we've made.

5.3.1 Transmission of Light in Atmospheric Conditions

One prominent challenge optical free-space links face is the effect of the atmosphere on the beam. Whereas absorption and scattering generally are unavoidable effects contributing to the overall attenuation of the beam intensity, fluctuations in the refractive index of the atmosphere cause beam wander and wavefront distortion that to some extent can — and need to — be compensated. Turbulent air is typically modeled through the statistical Kolmogorov model [72], where the turbulence is described phenomenologically by large *eddie* vortices at some outer scale $\mathcal{L}_0$, disintegrating into smaller eddies until the kinetic energy is dissipated due to viscosity at some inner scale l_0. The refractive index of the atmosphere is directly related to its density, which in turn fluctuates with the temperature and pressure changes due to the moving air. Eddie currents on the order of the free-space beam diameter consequently cause wavefront distortions on the millisecond scale, in turn causing angle of arrival (AoA) fluctuations in the beam. This can be observed as a jitter-motion of the beam spot at the receiving module, or as beam spread over longer exposure times. Larger eddies on the other hand cause beam wander over longer timescales. These angle of arrival fluctuations are essential to account for, as they limit the ability of the receiving telescope to image the beam onto the detector surface.

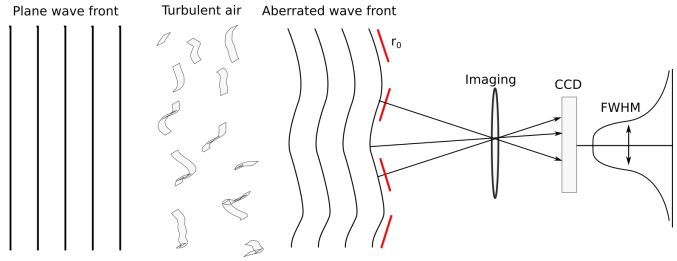

Figure 5.5: Illustration: Turbulent air cause wavefront distortions that is observed as beam spread in an imaging apparatus. The amount of turbulence can be quantified by the FWHM of the imaged beam spot.

A fundamental parameter for free-space links is the *atmospheric seeing*, ϵ_0. This can rudimentary be defined as the full-width half-maximum (FWHM) of a long-exposure image of a distant point-source. As the image of a distant point-source through the atmosphere is smeared out by the wavefront distortion (see Fig. 5.5), this is a measure of the AoA fluctuations caused by turbulence. A related quantity is the Fried parameter r_0 which can be considered as a characteristic size of turbulent cells in the atmosphere [73]. The two quantities are related to each other through

$$\epsilon_0 = 0.98\frac{\lambda}{r_0}, \tag{5.4}$$

where λ is the wavelength of the beam. For the design of the receiver telescope, it is important to keep in mind that this quantity competes with the diffraction limit of the

telescope aperture, as quantified by the Airy disk

$$FWHM_{\text{Airy}} = 1.028\frac{\lambda}{D}. \tag{5.5}$$

In the absence of any adaptive optics system compensating for the short-term wavefront distortions, the atmospheric turbulence will be the limiting factor of the imaging resolution as long as $r_0 < D$.

5.3.2 Differential Image Motion Monitoring (DIMM)

A widely used and convenient measurement setup for quantifying the Fried parameter is the Differential Image Motion Monitor (DIMM). A DIMM setup relates the Fried parameter to the variance of the relative beam spot motion of a point-source imaged over two apertures. This can be implemented with a single telescope system by placing a mask with two smaller apertures over the full aperture. A wedge prism in one of the apertures then deflects the corresponding wavefront to a different spot on the camera. Subsequent images of a point-source such as a star — or in our case a laser — over short exposure times then yield samples over how the distortion of the wavefront at the position of the two apertures changes relative to each other. After a series of short exposure images, the variance $(\sigma_d^2)_{l,t}$ in the longitudinal and transversal distance between the two beam spots can be related to the Fried parameter as [74]

$$(\sigma_d^2)_{l,t} = K_{l,t}\lambda^2 r_0^{-5/3} D^{-1/3}, \tag{5.6}$$

where D is the diameter of the subapertures, λ the wavelength of the point source and $K_{l,t}$ two constants dependent on the ratio of the diameter of the two apertures to the distance B between them. The longitudinal direction is here given as the direction parallel to the separation of the two apertures. From [74], these constants are given as

$$\begin{aligned} K_l &= 0.340(1 - 0.570b^{-1/3} - 0.040b^{-7/3}) \\ K_t &= 0.340(1 - 0.855b^{-1/3} - 0.030b^{-7/3}), \end{aligned} \tag{5.7}$$

where $b = B/D$. The distance between the two spots is calculated from the position of the centroid (center-of-intensity) of each beam spot. These coordinates are given by the weighted mean over the pixel-intensities in the image

$$(x_c, y_c) = \frac{\sum_{ij} p_{ij} I_{ij}}{\sum_{ij} I_{ij}}, \tag{5.8}$$

where p_{ij} are pixel coordinates and I_{ij} the corresponding intensity. I refer to [74] for a more detailed discussion on the DIMM method, as well as the relevant sources of error and potential pitfalls.

5.4 Setup and Design Choices

5.4.1 The Free-Space Link

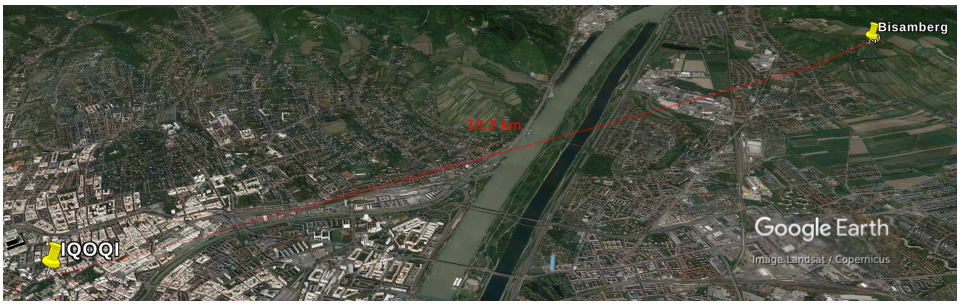

Figure 5.6: Satellite image over Donau showing the free-space link with the source and transmitter at the institute (IQOQI) and the receiving module at Bisamberg, 10.2 km away.

Fig. 5.6 shows the geographical location of our transmitter and receiver stations. The source and the Alice interferometer are placed in 4th floor laboratory at IQOQI Vienna, where the source can be coupled to a SM fiber going up to the transmitting optics at the rooftop cupola of the *Hedy Lamarr* telescope. The receiving station is installed in a room at the old *Sendeanlage Bisamberg*, belonging to the Austrian Broadcast Corporation (ORF). The physical link distance measures to $\sim 10.2\,\mathrm{km}$.

5.4.2 Transmitter Optics

For the transmitter optics, a SM fiber connected to the downstairs laboratory is mounted on a translation stage in front of an achromatic lens ($f = 274.5\,\mathrm{mm}$, $D = 70\,\mathrm{mm}$, LEnS-Optics). The lens is custom-made for a theoretical spot size with a Gaussian beam of $\sim 40\,\mathrm{cm}$ at $8\,\mathrm{km}$. The setup is mounted on the Hedy Lamarr telescope at the rooftop of IQOQI, depicted in Fig. 5.7, which can be rotated in order to aim at the receiver station.

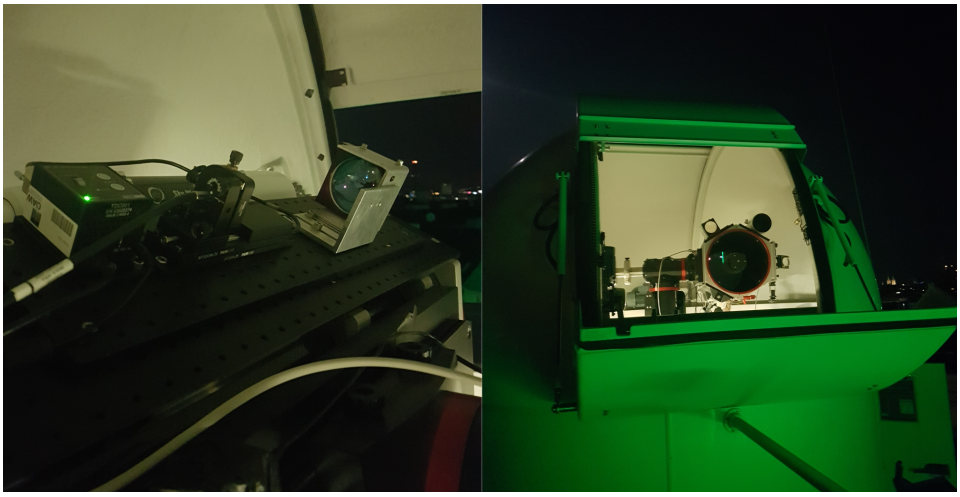

Figure 5.7: Image of the transmitting lens mounted on the Hedy Lamarr telescope, from inside and outside of the cupola. The green reflection on the cupola is from the nearby beacon LEDs used for the tracking setup.

5.4.3 Receiver Optics

The receiving optics are responsible for imaging the quantum signal transmitted through the atmosphere onto the detectors sensitive surface. In order to do so optimally, there are a series of consideration that need to taken. First of all, due to Gaussian beam divergence, the free-space signal must be collimated to a smaller size. The beam waist need to be smaller than $2.54\,\mathrm{cm}$, which is the diameter of all optics used inside the interferometer. This is done with a two lens collimation stage, which introduces a magnification M that shrinks the beam size and magnifies the AoA. As we will not use any real-time adaptive optics system to correct for the short-term AoA fluctuations caused by the atmosphere, the magnification should be small enough to still map these fluctuations onto the sensitive area of the detector. The angles that are successfully mapped to the detector surface are quantified by the *field of view* (FoV) of the detectors. However, this parameter also works as a spatial filter against noise and increasing it is therefore a trade-off in terms of noise robustness in QKD. Another issue is *beam clipping*, which occur when part of the beam path through the interferometer is obstructed. To minimize this effect, a small beam size is desirable. This in turn depends on the magnification, and is therefore another trade-off between the FoV. In terms of beam size, a final consideration that should be made is the *Rayleigh length* of the collimated beam, which is defined as the length over which the beam waist increases by a factor $\sqrt{2}$ due to Gaussian beam divergence. The Rayleigh length scales quadratically with the diameter of the collimated beam. As the total beam path from the telescope to the detector is quite long, this can be an issue if the beam size is too small.

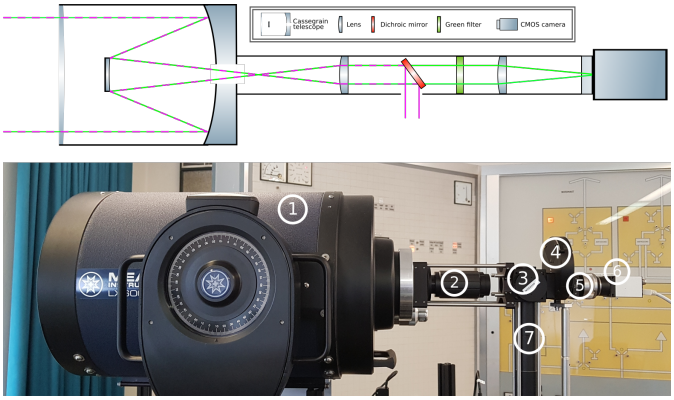

Figure 5.8: Image and schematic of the receiver optics. (1) Cassegrain telescope, (2) collimation lens, (3) dichroic mirror, (4) green filter, (5) focusing lens, (6) CMOS camera for tracking, (7) periscope leading into the interferometer.

The setup for our receiving optics is shown in Fig. 5.8. The main parts of which is the Cassegrain telescope (Meade LX600, $f = 2.032\,\mathrm{m}$, $D = 254\,\mathrm{mm}$) and the collimation lens (Thorlabs, Best Form lens, $f = 75\,\mathrm{mm}, D = 2.54\,\mathrm{cm}$). A dichroic mirror separates the quantum signal from the green beacon LEDs used for our tracking scheme. This is explained in more detail in Section 5.4.4. The effects of our design choices are calculated by using the standard theory of ray tracing matrices, valid for the paraxial region (see e.g. [22]). A table of the relevant parameters are listed in Table 5.1. For the clipping limit, I assume here a $3\,\mathrm{m}$ propagation distance, which gives some safety margin. These calculations are elaborated in more detail in Appendix A.

Table 5.1: Characteristic parameters of the receiver optics design.

Collimation stage	
Angular magnification	$\times 27.1$
Beam magnification	$\times 0.037$
Beam diameter after collimation	$9.4\,\mathrm{mm}$
Rayleigh range (@$810\,\mathrm{nm}$)	$342.6\,\mathrm{m}$
Clipping limit	$2.67\,\mathrm{mrad}$
Single-photon detector	
Focusing Lens	$50\,\mathrm{mm}$
Detector size	$180\,\mu\mathrm{m}$
Detecor FoV	$133\,\mu\mathrm{rad}$
Tracking camera	
Focusing Lens	$40\,\mathrm{mm}$
Pixel size	$5.5\,\mu\mathrm{m}$
Pixel FoV	$5.1\,\mu\mathrm{rad}$

5.4.4 Bidirectional Tracking

While the short-term AoA fluctuations caused by the atmosphere are compensated by the 4f system of the interferometer and the FoV of the detectors, active beam wander compensation is still essential for the long-term transmission stability of the link. We intend to compensate for this with a bidirectional tracking scheme, where green beacon LEDs positioned at the transmitter and receiver ends are used as references for the beam wander of the quantum signal[1]. The beacon LEDs are imaged by CMOS cameras (Baumer VLG–22M) at each side. At the transmitter station, we use the Hedy Lamarr telescope ($f = 1.140\,\mathrm{m}$, Astro Systeme Austria (ASA)) to focus on the beacon, while on the receiver side we use the same receiver optics as for the quantum signal, with a focusing lens ($f = 40\,\mathrm{mm}$, Thorlabs Best Form lens) placed after the transmitted arm of the dichroic mirror. The beam wander manifests itself as a moving beam spot on the image of the beacon LEDs. By calculating the averaged centroid position over a suitable time-frame, using Eq. 5.8, the motion of the centroid from one frame to the other can be compensated by adjusting the angles of the transmitter and receiver modules. For the transmitter, this is simply done by using the integrated motor of the telescope mount. For the receiver, we implement this by placing the entire optical setup on a 6-axis hexapod (PI Systems, H-850.H2), which is depicted in Fig. 5.9. The hexapod is able to carry up to $250\,\mathrm{kg}$, and can translate and rotate along all three cartesian axes. For the tracking, we use rotations in the horizontal and vertical directions (in relation to the incident beam), which can move in minimum increments of $5\,\mu\mathrm{rad}$ and $3\,\mu\mathrm{rad}$ respectively [75].

Tracking Algorithm The tracking algorithm is a simple feed-back loop, that tilts the setup in order to keep the centroid at a set reference position, which is determined at the start of the measurement when the interferometers are aligned. The CMOS camera has a wide dynamic range of exposure times, ranging from $15\,\mu\mathrm{s}$ to $1\,\mathrm{s}$, which can be used to find the suitable spot brightness. The centroid position is then measured in $1\,\mathrm{s}$ intervals (this is tunable in the software) as the average over a series of short exposure images. The corresponding pixel deviation from the reference position is then converted to a change in the AoA, which is compensated for by tilting the hexapod and the transmitter telescope correspondingly. This conversion factor is simply equal to the FoV of each camera pixel at the respective stations. For the receiver end, this value is $5.1\,\mu\mathrm{rad/pixel}$, while for the transmitter telescope the corresponding value is $4.82\,\mu\mathrm{rad/pixel}$.

Tracking Software The tracking is fully automated through software developed personally through this thesis work. It is implemented in the QT framework, and entails all the necessary functionalities for dealing with the CMOS camera, interfacing with the hexapod and the transmitter telescope and for setting up and performing DIMM measurements. This is described in more detail in Appendix B.

[1] The choice of using beacon LEDs instead of more powerful beacon lasers stem from a safety concern in regards to the nearby flight paths of ambulance helicopters.

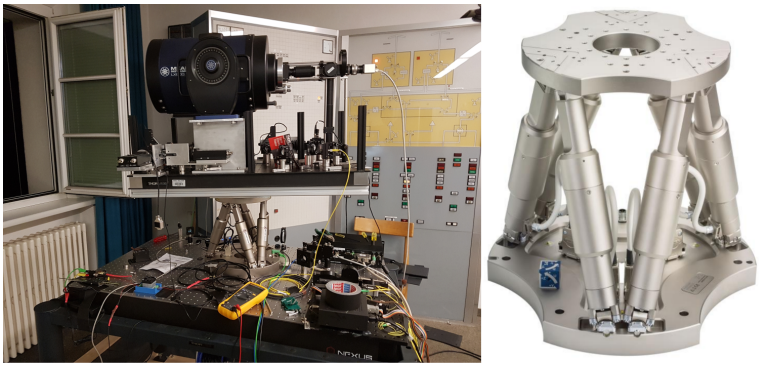

Figure 5.9: Picture of the complete receiver module, locked on the surface of a rotatable hexapod. The close-up image of the hexapod is taken from [75].

5.4.5 The DIMM Setup

Our receiver module can quickly turn into a DIMM device by placing the mask shown in Fig. 5.10 onto the telescope. The two apertures are $2.6\,\mathrm{cm}$ in diameter and separated by $16\,\mathrm{cm}$. Within one of these apertures, two $0.5°$ wedge prisms are fixed in rotatable mounts. This makes up a beam steering device which we use to displace the two beam spots. For the imaging, we use the same camera as for the tracking scheme. To perform a measurement, we shine a green laser from the transmitter optics, which is imaged in bursts over short exposure times. The exposure time and number of images per sample can be set in the software, which calculates and plots the seeing "real-time" (see Appendix B).

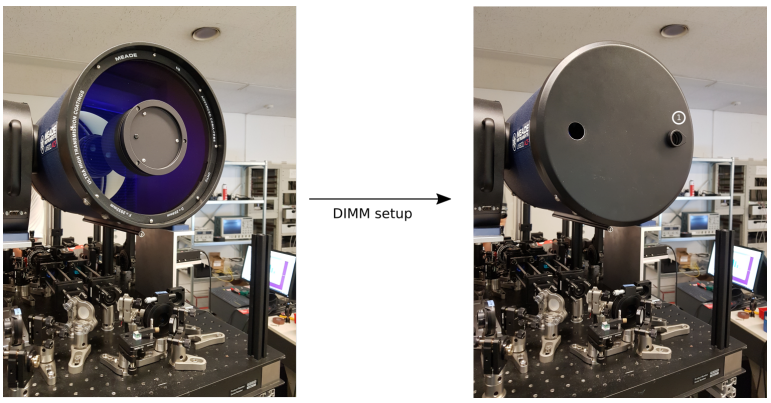

Figure 5.10: By placing a mask onto the receiver telescope, the setup is transformed into a DIMM setup. (1) Wedge prisms used for beam steering.

5.4.6 Test of the Tracking and DIMM Setup

The tracking and DIMM setup was tested during two brief runs on the night of 10.09.19. For the DIMM test, we used a green laser ($\lambda = 532\,\mathrm{nm}$) imaged in burst of 1000 images with an exposure time of $5\,\mathrm{ms}$. The measured Fried parameter and the corresponding atmospheric seeing is plotted over a $\sim 15\,\mathrm{min}$ measurement in Fig. 5.11. The relative statistical error in each estimation of the Fried parameter is equal to $\frac{3}{5}\sqrt{2/N}$ [76], corresponding to 2.7% for $N = 1000$. At this point, biases due to CCD read-out noise, photon noise and exposure time averaging are likely more influential [74]. The average seeing over this short measurement was $43.55\,\mu\mathrm{rad}$. As the Fried parameter scales with the wavelength as $r_0 \propto \lambda^{6/5}$, the atmospheric seeing of the $810\,\mathrm{nm}$ quantum signal should be better by a factor $\epsilon_0(810\,\mathrm{nm}) = 0.6\epsilon_0(532\,\mathrm{nm})$. This magnitude of the AoA fluctuations are well handled by the receiver optics. Generally, this value will vary from day to day however, so it is not possible to assess a general range of the expected fluctuations from this short measurement.

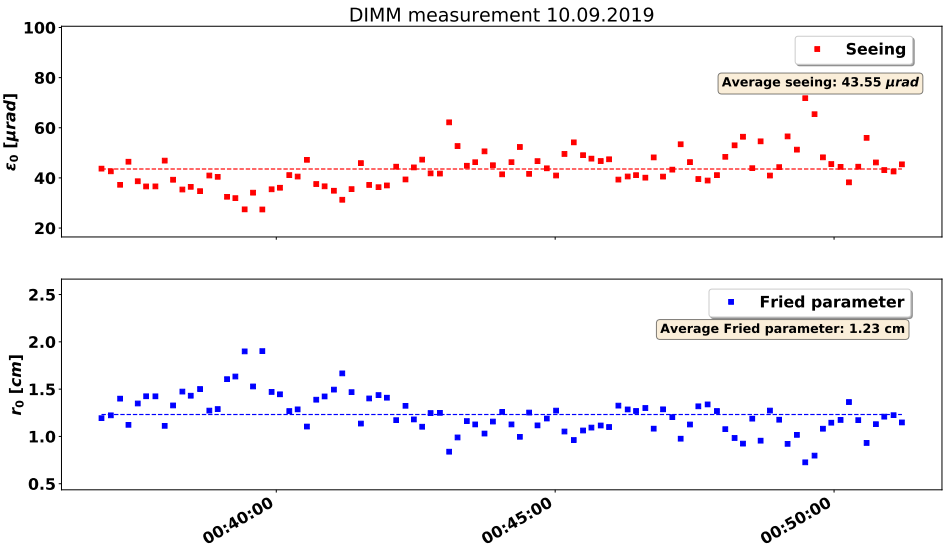

Figure 5.11: DIMM measurement over $\sim 15\,\mathrm{min}$ the night of 10.09.19. Each point corresponds to 1000 images with $5\,\mathrm{ms}$ exposure time.

The transmission stability of the link was subsequently tested by shining a $775\,\mathrm{nm}$ laser from the transmitting optics, while the tracking system focused on the green beacon LEDs. However, due to continued software issues with the transmitter telescope, active tracking could only be tested with the hexapod at the time of these measurements. For this test, the centroid spot of the beacon LED was averaged over $1\,\mathrm{s}$ intervals before prompting a move by the hexapod. The deviation of these centroids in pixels from the initial position at the start of the measurement is plotted in Fig.5.12, along with the measured attenuation of the beam. The attenuation is calculated as

$$\text{Attenuation [dB]} = 10 \log_{10} \frac{\text{Input power}}{\text{Output power}}, \tag{5.9}$$

where the output power was measured at the end of the periscope of the receiver optics (see Fig. 5.8). The input power was measured at the start of the measurement to $16\,\mathrm{mW}$, and assumed constant throughout.

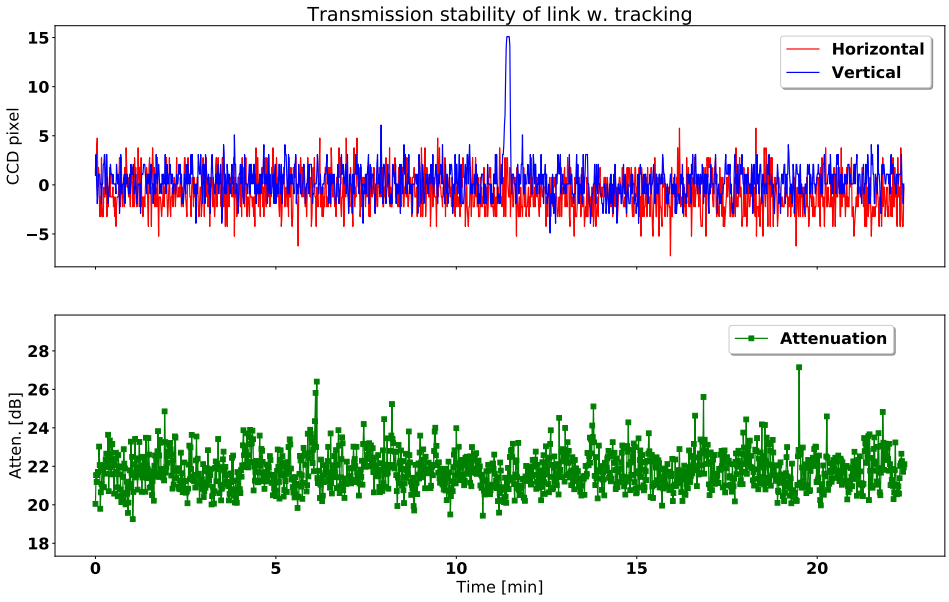

Figure 5.12: The transmission stability of the one-way tracking scheme was tested. At the top, the horizontal and vertical motion of the centroid of the beacon LED is plotted. At the bottom, the link attenuation during the same time.

It is difficult to give a well reasoned assessment of the tracking setup from this short measurement — especially with only one active side — but in the least it shows that the feed-back loop is stable, keeping the beam spot and the transmission power oscillating around a mean value. However, as the sensor area of the power meter is much larger than the single-photon detectors, it is probable that the attenuation will have larger fluctuations when we do the same test with the quantum signal. This is likely also the reason why the central peak of the vertical pixel deviation did not substantially affect the attenuation, which for the record was caused by walking across the room of the receiver module, as there the floor is quite unsteady. Nevertheless, these results give reason to believe that any additional issues in the transition to the quantum signal can be overcome by small tweaks to the tracking parameters.

Chapter 6

Summary and Outlook

Quantum entanglement will be a central resource in the next generation of quantum technologies. Motivated by this, I used this thesis to explore theoretical concepts and experimental techniques for producing, manipulating and verifying entanglement in two-photon systems. Utilizing these fundamental tools, I describe two experiments I've contributed to at the Institute for Quantum Optics and Quantum Information in Vienna.

The first experiment is described in Chapter 4, and is related to the use of entangled photons for remote clock synchronization. The concept can be broken into two key ideas: First of all, photon pairs produced through SPDC are temporally correlated within less than $1\,\mathrm{ps}$. Secondly, the error in timing resolution due to electronic jitter can be made arbitrarily small with the statistics provided by bright SPDC sources. Consequently, the relative clock drift between two remote clocks can be asserted over relatively small sampling times by the drift of the time offset of the two-photon coincidence peak. In terms of QKD protocols, this is already an established technique to improve the clock synchronization between the sender and receiver beyond the possible precision obtained by pulse-per-second GPS signals. I here rather investigate this scheme as a tool for time and frequency metrology, in this instance specifically oriented towards measuring gravitational time dilation. This is first of all an interesting angle as a series of QKD satellites likely will be launched in the upcoming years, in which the time dilation effects approach the order of magnitude accessible by this synchronization scheme. Furthermore, few extra modifications would in principle be needed for these setups, as this tool is intrinsically available in any entanglement-based QKD setup. To test this principle, we measured the fractional frequency drift of two freely running rubidium standard atomic clocks over three consecutive long-term intervals ($> 13\,\mathrm{h}$). During the second measurement, one of the clocks were lifted to a height of $4\,\mathrm{m}$, to see if time dilation effects could become visible. With coincidence rates in the order of $100\,\mathrm{kcps}$, the fractional frequency deviation was measured to

a theoretical precision of $1\,\mathrm{ps}$ over sampling times of $1\,\mathrm{s}$, where the $1\,\mathrm{ps}$ counting resolution of the time tagger units set the fundamental limit of the obtainable precision. Over averaging times from $1\,\mathrm{s}$ to $10\,000\,\mathrm{s}$, the Allan deviation of the two clocks was measured to $\sim 10^{-11}$, which is in reasonable agreement with the claimed stability of the clocks. However, as this is far above the frequency shift predicted by gravity, we could not certify time dilation from the $4\,\mathrm{m}$ height difference with this setup. Nevertheless, this is mainly an issue with the stability of the clocks, and we demonstrate that the fundamental principle of the clock synchronization scheme is sound. Whether it is possible to use this for metrology in future LEO QKD satellites would be premature to conclude, as the effects of lower coincidence counts and increased path length variations likely worsen the synchronization precision by some order of magnitude.

The design choices and preparatory measurements for a free-space QKD setup was investigated in Chapter 5. This experiment is the next step in a series of projects [70, 77] intended to demonstrate the feasibility of higher-dimensional entanglement for a noise robust QKD protocol. This protocol relies on two post-selection free Franson interferometers to analyze the higher-dimensional state-space offered by photons entangled in polarization and energy-time. At the current time, the entangled photon source and the two interferometer modules have been tested locally in the lab, demonstrating a Franson interference of 92%, and the setup is in the process of being prepared for free-space tests. In terms of this, ensuring the transmission stability of the link despite the effects of atmospheric turbulence is a prominent engineering challenge. The limitations of turbulence across our link is assessed with a differential image motion monitor (DIMM) integrated in the receiver module. In a test of this setup, the atmospheric seeing was measured with a green laser to an average of $43.55\,\mu\mathrm{rad}$ over $\sim 15\,\mathrm{min}$. These short-term fluctuations are accounted for in the design of the receiver optics, primarily by the addition of two 4f lens systems in the long arms of the interferometer, and by selecting a larger field of view than the expected angle of arrival fluctuations for the single-photon detectors. For the long-term stability of the link, I presented a setup for a bidirectional tracking scheme, correcting the angle of our transmitter module and receiver module in a closed feed-back loop to ensure optimal transmission stability. However, due to software issues with the transmitter telescope, only the tracking setup for the receiver end was possible to test during this thesis work. At the current time, this experiment is at the exciting stage where we start observing interference with an alignment laser across the free-space link, and therefore expect to demonstrate Franson interference in the not-so-distant future. Succeeding in demonstrating a noise robust QKD protocol over a $10.2\,\mathrm{km}$ long free-space link will likely be a significant contribution to the development of QKD for global networks.

Bibliography

[1] Kristian Hjorth. "Theoretical Background of a Bell Inequality Test for Polarization and Energy-Time Entangled Photons", 2019. Project thesis. Available upon request.

[2] J. S. Bell. "On the Einstein Podolsky Rosen paradox". *Physics Physique Fizika*, 1:195–200, Nov 1964.

[3] Alain Aspect, Philippe Grangier, and Gérard Roger. "Experimental Tests of Realistic Local Theories via Bell's Theorem". *Phys. Rev. Lett.*, 47:460–463, Aug 1981.

[4] Stuart J. Freedman and John F. Clauser. "Experimental Test of Local Hidden-Variable Theories". *Phys. Rev. Lett.*, 28:938–941, Apr 1972.

[5] W. Tittel et al. "Experimental Demonstration of Quantum Correlations over more than 10 km". *Phys. Rev. A*, 57:3229–3232, May 1998.

[6] Dominik Rauch et al. "Cosmic Bell Test Using Random Measurement Settings from High-Redshift Quasars". *Phys. Rev. Lett.*, 121:080403, Aug 2018.

[7] M. Giustina et al. "Bell violation with entangled photons, free of the fair-sampling assumption". In *2013 Conference on Lasers Electro-Optics Europe International Quantum Electronics Conference CLEO EUROPE/IQEC*, pages 1–1, May 2013.

[8] Gregor Weihs et al. "Violation of Bell's inequality under strict Einstein locality conditions". *Phys. Rev. Lett.*, 81:5039–5043, 1998.

[9] J. Brendel, E. Mohler, and W. Martienssen. "Experimental Test of Bell's Inequality for Energy and Time". *EPL (Europhysics Letters)*, 20(7):575, 1992.

[10] J. G. Rarity and P. R. Tapster. "Experimental Violation of Bell's Inequality Based on Phase and Momentum". *Phys. Rev. Lett.*, 64:2495–2498, May 1990.

[11] A. Mair, A. Vaziri, G. Weihs, and A. Zeilinger. "Entanglement of the Orbital Angular Momentum States of Photons". *Nature*, 412:313–316, July 2001.

[12] Julio T. Barreiro et al. "Generation of Hyperentangled Photon Pairs". *Phys. Rev. Lett.*, 95:260501, Dec 2005.

[13] B. Hensen et al. "Loophole-free Bell inequality violation using electron spins separated by 1.3 kilometres". *Nature*, 526:682–686, 2015.

[14] H. Bernien et al. "Heralded entanglement between solid-state qubits separated by three metres". *Nature*, 497(7447):86–90, May 2013.

[15] Ming Gong et al. "Genuine 12-Qubit Entanglement on a Superconducting Quantum Processor". *Physical Review Letters*, 122(11):110501, Mar 2019.

[16] Gary J. Mooney, Charles D. Hill, and Lloyd C. L. Hollenberg. "Entanglement in a 20-Qubit Superconducting Quantum Computer". *arXiv e-prints*, page arXiv:1903.11747, Mar 2019.

[17] Roy Glauber. *The Quantum Theory of Optical Coherence*. Wiley-VCH Verlag GmbH & Co. KGaA, 2007.

[18] Christopher Gerry and Peter Knight. *Introductory Quantum Optics*. Cambridge University Press, 2004.

[19] Mark Fox. *Quantum Optics: An Introduction*. Oxford University Press, 2006.

[20] Leonard Mandel and Emil Wolf. *Optical Coherence and Quantum Optics*. Cambridge University Press, 1995.

[21] Karl-Peter Marzlin. *Quantum Optics and Nonlinear Optics*. University of Calgary, 2007.

[22] Bahaa E. A. Saleh and Malvin Carl Teich. *Fundamentals of Photonics; 2nd ed.* Wiley series in pure and applied optics. Wiley, New York, NY, 2007.

[23] Albert Einstein. "Concerning an Heuristic Point of View Toward the Emission and Transformation of Light". *Annalen Phys.*, 17:132–148, 1905.

[24] Zheyu Jeff Ou. *Quantum Optics for Experimentalists*. World Scientific, 2017.

[25] Charles H. Bennett and Gilles Brassard. "Quantum cryptography: Public key distribution and coin tossing". *Theor. Comput. Sci.*, 560:7–11, 2014.

[26] S. P. Walborn et al. "Double-slit quantum eraser". *Phys. Rev. A*, 65(3):033818, Mar 2002.

[27] B. Brecht et al. "Photon Temporal Modes: A Complete Framework for Quantum Information Science". *Phys. Rev. X*, 5:041017, Oct 2015.

[28] Alex O. C. Davis, Valérian Thiel, Michał Karpiński, and Brian J. Smith. "Measuring the Single-Photon Temporal-Spectral Wave Function". *Physical Review Letters*, 121(8):083602, Aug 2018.

[29] Benjamin Brecht et al. "From quantum pulse gate to quantum pulse shaper—engineered frequency conversion in nonlinear optical waveguides". *New Journal of Physics*, 13(6):065029, Jun 2011.

[30] Manuel Erhard et al. "Twisted photons: new quantum perspectives in high dimensions". *Light: Science & Applications*, 7(3):17146–17146, 2018.

[31] John F. Clauser, Michael A. Horne, Abner Shimony, and Richard A. Holt. "Proposed Experiment to Test Local Hidden-Variable Theories". *Phys. Rev. Lett.*, 23:880–884, Oct 1969.

[32] A. Einstein, B. Podolsky, and N. Rosen. "Can Quantum-Mechanical Description of Physical Reality Be Considered Complete?". *Phys. Rev.*, 47:777–780, May 1935.

[33] The Big Bell Test Collaboration. "Challenging local realism with human choices". *Nature*, 557(7704):212–216, 2018.

[34] Otfried Gühne and Géza Tóth. "Entanglement detection". *Physics Reports*, 474(1-6):1–75, Apr 2009.

[35] T. D. Ladd et al. "Quantum computers". *Nature*, 464(7285):45–53, Mar 2010.

[36] Thomas Herbst et al. "Teleportation of entanglement over 143 km". *Proceedings of the National Academy of Science*, 112(46):14202–14205, Nov 2015.

[37] V. Scarani et al. "The security of practical quantum key distribution". *Reviews of Modern Physics*, 81:1301–1350, July 2009.

[38] Fabian Steinlechner. *Sources of Photonic Entanglement for Applications in Space*. PhD thesis, ICFO, 2015.

[39] Z.-Y. J. Ou. *Multi-Photon Quantum Interference*. Springer-Verlag US, 2007.

[40] Morton H. Rubin et al. "Theory of two-photon entanglement in type-II optical parametric down-conversion". *Phys. Rev. A*, 50:5122–5133, Dec 1994.

[41] Paul G. Kwiat. "Hyper-entangled states". *Journal of Modern Optics*, 44(11-12):2173–2184, 1997.

[42] M. V. Jabir and G. K. Samanta. "Robust, high brightness, degenerate entangled photon source at room temperature". *Scientific Reports*, 7(1):12613, 2017.

[43] Sebastian Ecker. "Hyperentangled photon pairs for free-space quantum communication". Master's thesis, Technische Universität, Wien, 2016.

[44] J. D. Franson. "Bell inequality for position and time". *Phys. Rev. Lett.*, 62:2205–2208, May 1989.

[45] Mark Brezinski. "A Quantum Field Approach for Advancing Optical Coherence Tomography Part I: First Order Correlations, Single Photon Interference, And Quantum Noise". *Journal of Lasers, Optics & Photonics*, 05, 02 2014.

[46] Yoon-Ho Kim. "Measurement of one-photon and two-photon wave packets in spontaneous parametric downconversion". *Journal of the Optical Society of America B Optical Physics*, 20(9):1959–1966, Sep 2003.

[47] Jan-Ake Larsson, Sven Aerts, and Marek Zukowski. "Two photon Franson type interference experiments are not tests of local realism". *arXiv e-prints*, 1998.

[48] A. Cabello et al. "Proposed Bell Experiment with Genuine Energy-Time Entanglement". *Physical Review Letters*, 102(4):040401, January 2009.

[49] D. V. Strekalov et al. "Postselection-free energy-time entanglement". *Phys. Rev. A*, 54:R1–R4, July 1996.

[50] Nathan Langford. *Encoding, manipulating and measuring quantum information in optics*. PhD thesis, University of Queensland, 2019.

[51] Caleb Ho, Antía Lamas-Linares, and Christian Kurtsiefer. "Clock synchronization by remote detection of correlated photon pairs". *New Journal of Physics*, 11(4):045011, Apr 2009.

[52] Alejandra Valencia, Giuliano Scarcelli, and Yanhua Shih. "Distant clock synchronization using entangled photon pairs". *Applied Physics Letters*, 85(13):2655, Sep 2004.

[53] Runai Quan et al. "Demonstration of quantum synchronization based on second-order quantum coherence of entangled photons". *Scientific Reports*, July 2016.

[54] Jianwei Lee et al. "Symmetrical clock synchronization with time-correlated photon pairs". *Applied Physics Letters*, 114(10):101102, Mar 2019.

[55] Sheng-Kai Liao et al. "Satellite-Relayed Intercontinental Quantum Network". *Phys. Rev. Lett.*, 120:030501, Jan 2018.

[56] Erik Kerstel et al. "Nanobob: A Cubesat Mission Concept For Quantum Communication Experiments In An Uplink Configuration". *arXiv e-prints*, page arXiv:1711.01886, Nov 2017.

[57] Sebastian Philipp Neumann et al. "Q3Sat: quantum communications uplink to a 3U CubeSat–feasibility & design". *EPJ Quantum Technology*, 5(1):4, 2018.

[58] Daniel KL Oi et al. "CubeSat quantum communications mission". *arXiv e-prints*, page arXiv:1704.08707, Apr 2017.

[59] M. Aspelmeyer et al. "Long-distance quantum communication with entangled photons using satellites". *IEEE Journal of Selected Topics in Quantum Electronics*, 9(6):1541–1551, Nov 2003.

[60] C. W. Chou et al. "Optical Clocks and Relativity". *Science*, 329(5999):1630–1633, 2010.

[61] J. C. Hafele and Richard E. Keating. "Around-the-World Atomic Clocks: Predicted Relativistic Time Gains". *Science*, 177(4044):166–168, 1972.

[62] Michael Lombardi. "Fundamentals of Time and Frequency". In *The Mechatronics Handbook*, chapter 17. CRC Press, 2002.

[63] Stanford Research Systems. *FPS740 GPS Time and Frequency System*. User Manual. Version 1.05. January 15, 2019.

[64] Gregor Weihs. *Ein Experiment zum Test der Bellschen Ungleichung unter Einsteinscher Lokalitat*. PhD thesis, University of Vienna, 1998.

[65] Neil Ashby. "Relativity in the Global Positioning System". *Living Reviews in Relativity*, 55, 2003.

[66] T C Ralph and J Pienaar. "Entanglement decoherence in a gravitational well according to the event formalism". *New Journal of Physics*, 16(8):085008, aug 2014.

[67] Heasin Ko et al. "Experimental filtering effect on the daylight operation of a free-space quantum key distribution". *Scientific Reports*, 8(1):15315, 2018.

[68] Matthew P. Peloso et al. "Daylight operation of a free space, entanglement-based quantum key distribution system". *New Journal of Physics*, 11(4):045007, Apr 2009.

[69] Yun-Hong Gong et al. "Free-space quantum key distribution in urban daylight with the SPGD algorithm control of a deformable mirror". *Opt. Express*, 26(15):18897–18905, Jul 2018.

[70] Sebastian Ecker et al. "Entanglement distribution beyond qubits or: How I stopped worrying and learned to love the noise". *arXiv e-prints*, Apr 2019.

[71] Jeongwan Jin et al. "Demonstration of analyzers for multimode photonic time-bin qubits". *Phys. Rev. A*, 97:arXiv:1509.07490, Sep 2015.

[72] A. N. Kolmogorov. "The Local Structure of Turbulence in Incompressible Viscous Fluid for Very Large Reynolds Numbers". *Proceedings: Mathematical and Physical Sciences*, 434(1890):9–13, 1991.

[73] D. L. Fried. "Optical Resolution Through a Randomly Inhomogeneous Medium for Very Long and Very Short Exposures". *J. Opt. Soc. Am.*, 56(10):1372–1379, Oct 1966.

[74] A. Tokovinin. "From Differential Image Motion to Seeing". *Publications of the Astronomical Society of the Pacific*, 114(800):1156, 2002.

[75] Physik Instrumente. *6-axis Hexapod*. User Manual. Version 2.4.4. June 22, 2018.

[76] V. Kornilov et al. "Combined MASS-DIMM instruments for atmospheric turbulence studies". *Monthly Notices of the Royal Astronomical Society*, 382(343):1268–1278, Dec 2007.

[77] Fabian Steinlechner et al. "Distribution of high-dimensional entanglement via an intra-city free-space link". *Nature Communications*, 8, 2017.

Appendix A

Some Classical Optics

The receiver optics was designed using the classical theory of ray transfer matrices, which typically is valid in the paraxial approximation, i.e. where the incoming light is nearly parallel with the optical axis of the system. In this formalism, the height and angle of a light ray is described by a vector $\mathbf{r} = \begin{pmatrix} r \\ \theta \end{pmatrix}$, and transfer matrices traces the ray through the system. Free space propagation and thin lenses is described by matrices $\mathbf{T}(d)$ and $\mathbf{L}(f)$ respectively, where

$$\mathbf{T}(d) = \begin{pmatrix} 1 & d \\ 0 & 1 \end{pmatrix}, \quad \mathbf{L}(f) = \begin{pmatrix} 1 & 0 \\ \frac{-1}{f} & 1 \end{pmatrix}. \tag{A.1}$$

A frequently encountered setup is the two-lens system with respective focal lenghts f_1, f_2, where the second lens is placed in a distance $f_1 + f_2$ from the first one. This is for example used for the collimation stage of the receiver optics. The angular magnification, M, of this setup is given by

$$M = \frac{f_1}{f_2}. \tag{A.2}$$

The beam size magnification is correspondingly given by the inverse of M. An important parameter in our receiver optics design is the *Field of View* (FoV) of the tracking camera and the single photon detectors. For a detector with diameter d_{det} placed in the image plane of lens with focal length f_3 after a two-lens system, the FoV is given by

$$FoV = \frac{d_{det}}{M f_3}. \tag{A.3}$$

Using the ray tracing matrices, it is straightforward to derive the features of the 4f system used for the receiver interferometer. The transformation of the first 4f system is

$$\mathbf{S}_{4f} = \mathbf{T}(f_2)\mathbf{L}(f_2)\mathbf{T}(f_1+f_2)\mathbf{L}(f_1)\mathbf{T}(f_1) = \begin{pmatrix} -M & 0 \\ 0 & -\frac{1}{M} \end{pmatrix}, \tag{A.4}$$

where M is the magnification caused by the two lenses. Placing a second 4f system with the order of the lenses reversed, we then obtain the identity mapping

$$\mathbf{S}_{4f}\mathbf{S}_{4f}^{-1} = \begin{pmatrix} -M & 0 \\ 0 & -\frac{1}{M} \end{pmatrix} \begin{pmatrix} -\frac{1}{M} & 0 \\ 0 & -M \end{pmatrix} = \mathbb{1}. \tag{A.5}$$

Thus, the two 4f systems is equivalent to a one-to-one mapping of the incident angle and height of the beam to the focal plane of the last lens.

Beam clipping occurs when part of the beam is obstructed. If we assume the aperture diameter, a, stays constant throughout the receiver optics and interferometer, beam clipping occurs at some critical angle θ_c corresponding to

$$L \sin\theta_c + \frac{d}{2} = \frac{a}{2}, \tag{A.6}$$

where L is the maximal propagation length and d is the beam diameter. Of course, if there are various apertures sizes throughout the setup, the critical angle will depend on where along the beam path these are positioned.

Gaussian Beams The beam waist, w, of a Gaussian beam diverges according to

$$w(z) = w_0\sqrt{1+\frac{z^2}{z_R^2}}, \tag{A.7}$$

where w_0 is the beam waist at its narrowest point, z is the propagation distance and z_R is the *Rayleigh range*. The Rayleigh range is defined as the length over which the beam radius increases by a factor $\sqrt{2}$. This length is given by

$$z_R = \frac{\pi w_0^2}{\lambda}, \tag{A.8}$$

where λ is the wavelength.

Appendix B

Tracking Software

In order to handle the bidirectional tracking for the free-space link, it was necessary to develop a software application, interfacing between the CMOS camera and the hexapod and transmitter telescope. Additionally, an application for the DIMM measurement was integrated into the software. I here provide some brief documentation.

Dependencies In addition to standard QT and C++ libraries, the application utilizes product specific software libraries to interface with the Baumer CMOS camera and the PI Hexapod. Images from the CMOS camera are handled with the opencv library.

Setup specific parameters Parameters specific to the setup and the components are written into the header file *datacontainers.h*. Here, containers handling the thread-safe sharing of data between the applications are stored. Perhaps more importantly for eventual second hand users, this file contains structs defining parameters specific to the setup, such as the receiver optics, hexapod, transmitter telescope and camera.

GUI Hierarchy

The main GUI thread, *TrackingGui*, handles the interplay between the four main functionalities. Within this application window (see Fig. B.1), connections to the camera, the hexapod and the transmitter telescope is established, as well as thread-safe sharing of data between the applications. Following is a description of the four main applications, and their functionalities within the software.

CameraGui Handles the interface with the Baumer GAPI SDK. All processes run by the

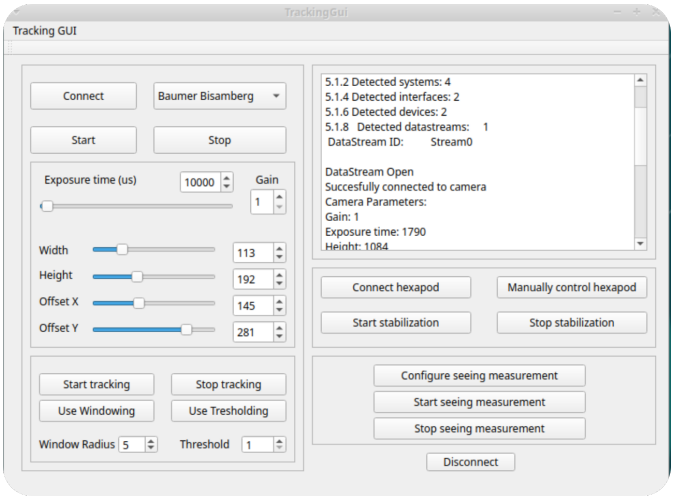

Figure B.1: Screenshot of the TrackingGui.

CameraGui is controlled through the main TrackingGui. This includes establishing a connection to the camera, initalizing a data stream, live display of the images, termination of the data stream and termination of the camera connection. Changes in the camera parameters are set in the TrackingGui, and subsequently handled by the CameraGui. Adjustable camera parameters include the exposure time, the gain and the sensitive detector area, which is set with the width, height and x and y offset commands. Additionally, the CameraGui handles the live calculation of image centroids, which are shared with HexapodGui (or HedyLamarrGui) during tracking. In the case of a seeing measurement, the images themselves are shared with the SeeingGui.

HexapodGui Handles the interface with the PI API. Within the TrackingGui, the connection to the hexapod can be established, which subsequently will perform a reference move to determine its absolute position. Successful connection to the hexapod opens up the HexapodGui window, where the position of the hexapod is shown in the tool and work system coordinates (see the Hexapod user manual for further explanation). Within the Gui, one can operate with two different coordinate systems. The standard *ZERO* system defines absolute positions relative to the standard coordinate system of the hexapod. Additionally, one can choose to set the active coordinate system to *USERDEFINED*, which uses the current position as origo. Manual movement of the hexapod can either be commanded through the *move to position* button, which moves to the coordinates typed into the corresponding text windows, or by using the keyboard to move in increments. The latter mode must be set via the TrackingGui. Lastly, the stabilization mode used during the bidirectional tracking can be activated in the TrackingGui. This disables all manual motion commands. During this mode, a graph window shows the motion of the hexapod and the centroid deviations (see Fig. B.2). This data is automatically stored.

Important note: before using the hexapod for tracking, set the active coordinate system

to USERDEFINED at the current position when the free-space link is aligned. Tilts are then defined relative to this coordinate system.

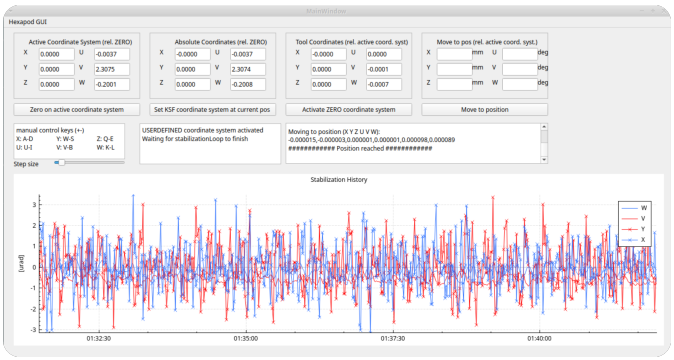

Figure B.2: Screenshot of the HexapodGui.

SeeingGui The SeeingGui handles the settings and calculations for a DIMM measurement. This window is opened via the TrackingGui, which also handles the start and termination of the measurement. Within the SeeingGui, the sample number and the window radius used in the centroid algorithm can be set. Also, the path to a suitable storage folder for images and calculations can be defined. Before starting a measurement, suitable camera parameters must be set with the TrackingGui, the aperture mask must be placed on the setup and the two beam steering prisms must be rotated into a position where both spots are visible on the camera. The atmospheric seeing and the Fried parameter is calculated "real-time" and displayed on the corresponding graphs in the GUI window (see Fig. B.3).

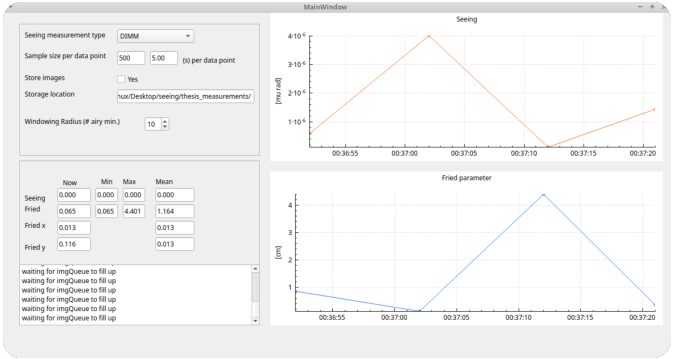

Figure B.3: Screenshot of the SeeingGui.

HedyLamarrGui The HedyLamarrGui is mostly duplicated code from the HexapodGui. The main difference is the interface to the telescope itself, which is implemented through a QSocket connection. The interface with the telescope has had quite a few issues however, as the offset commands are prone to adjustments from the ASA team.

NTNU
Norwegian University of
Science and Technology